Technische
Universität
München

Walther - Meißner -
Institut für Tief -
Temperaturforschung

Bayerische
Akademie der
Wissenschaften

Quantum Memory with Optimal Control

Master Thesis

Stephan Trattnig

Supervisor: Prof. Dr. Rudolf Gross

München, Mai 2020

Fakultät für Physik
Technische Universität München

Contents

Chapter 1

Introduction

Throughout the last decades, quantum technology evolved to a field with numerous of potential applications [1]. The subfield of quantum information processing aims at providing new technology for communication and computing. Whilst communication tasks would mainly benefit from a security perspective [2], quantum computing allows for solving certain computational problems substantially faster than classical computers [3–5]. One of the most promising architectures for enabling quantum computing are devices based on superconducting quantum circuits [6, 7]. With multi-qubit experiments operating up to 53 physical qubits [8], the question of improving single qubit performance is still an active area of research. It is split into two parts, namely the improvement of fabrication and the improvement of control. Whilst fabrication focuses on better qubit geometries and material, the field of control aims at improving the fidelity of quantum operations.

The focus of this work lies in optimizing the control of a 3D quantum memory. Our sample fabricated by E. Xie [9, 10] already proved to work as memory swapping a qubit state into and out of a resonator. In contrast to other memory experiments [11], the memory approach using 3D cavity modes as coupled resonators for storage and readout purposes benefits from long coherence times which are related to the high Q-factor of superconducting 3D cavities [12].

Built on the work of E. Xie, this work is a first step in introducing concepts of quantum optimal control to our quantum memory experiment. Quantum optimal control is a class of optimization techniques linked to the mathematical field of optimal control [13–15]. The aim of optimal control is to efficiently drive a dynamical quantum system from a given initial state to a desired target state with respect to boundary conditions. It includes optimizing the drive pulse envelopes as well as applying more sophisticated pulse shapes that predict improvements from a theory point of view [16, 17].

Throughout this work, we implement a communication interface allowing us to operate our quantum memory experiment independent of the already established and rigid device control in LabView. Shifting our pulse control to python provides us with the full variety of optimization techniques developed by our theory collaborators S. Machnes and N. Wittler from Saarland University. Pulseshapes can now be defined on a nanoscale resolution. As a first proof to show the superiority of our strategy, we apply our optimization scheme to simple pulses struggling for the optimum between shortness desired for applicable gates and length desired for suppressing state leakage. For the qubit pulse, a process tomography implemented by M. Renger [18] shows noticeable improvements. Further progress of testing and optimizing the full memory protocol is expected in future experiments.
This work ist structured as follows. In chapter 2, we introduce fundamental theory and measurement protocols relevant for this thesis. Chapter 3 is divided into two parts. The first one, Sec. 3.1, explains our experiment from a technical point of view. This section includes a description of the sample, the cryogenic wiring, the pulse generation setup, and the readout via an FPGA-enhanced digitizer card. In Sec. 3.2, we provide the reader with measurements characterizing our sample. We present our results on optimized drive pulses for our quantum memory in chapter 4, starting with a detailed description of our optimal control engine in Sec. 4.1. We then show first proof of concept results of optimizing qubit and blue sideband π-pulses in Sec. 4.2. In Sec. 4.3, the improved qubit π-pulse fidelity is proven by quantum process tomography. Finally, in Sec. 4.4, we present preliminary results on the memory protocol itself.

Chapter 2

Theory

2.1 Quantum information theory

In this section, the fundamental concepts of quantum bits and quantum gates are introduced from an information theory point of view. They are essential for any quantum computing logic.

2.1.1 Quantum bit

The basic unit of classical information theory is the bit [19]. Necessary for the physical implementation of such a classical bit is any system allowing for two distinguishable states. In information theory, these states are referred to as "0" - state or "1" - state and can have various physical implementations.
For quantum computing purposes, the quantum bit (qubit) is the basic unit of information [20]. Similarly to its classical counterpart, a qubit is defined over a basis consisting of two distinguishable states. Due to the quantum nature, superpositions are possible between the $|0\rangle$ - state and $|1\rangle$ - state. An arbitrary pure quantum state is defined as [21]

$$|\psi\rangle = \alpha\,|0\rangle + \beta\,|1\rangle\,, \tag{2.1}$$

where α and β are complex coefficients. The normalization condition for quantum states implies $|\alpha|^2 + |\beta|^2 = 1$ which reduces the number of free real parameters to two. The qubit state in general is not unique since any global phase $e^{i\Phi}$ does not alter the state. Due to those conditions, we can rewrite Eq. (2.2) to

$$|\psi\rangle = \cos\frac{\theta}{2}\,|0\rangle + e^{i\varphi}\sin\frac{\theta}{2}\,|1\rangle\,, \tag{2.2}$$

where $\theta \in [0, \pi]$ and $\varphi \in [0, 2\pi]$ are real parameters. Using a vector notation, the

states can be expressed as [21]

$$|0\rangle = \begin{pmatrix} 1 \\ 0 \end{pmatrix} \qquad |1\rangle = \begin{pmatrix} 0 \\ 1 \end{pmatrix} \qquad |\psi\rangle = \begin{pmatrix} \cos\frac{\theta}{2} \\ e^{i\varphi}\sin\frac{\theta}{2} \end{pmatrix}. \tag{2.3}$$

The vector notation is useful but only possible for pure states. In real-world physics, coupling to environment leads to a loss of information about the qubit state (cf. Sec. 2.4.2). This leads to mixed qubit states which need to be described as statistical ensembles of pure states. We can write both, pure and mixed qubit states using the density matrix notation

$$\rho = \sum_i p_i \left|\psi_i\right\rangle \left\langle\psi_i\right|, \tag{2.4}$$

where $\sum_i p_i = 1$ and $p_i \geq 0$. Mixed states and pure states both fulfill the trace condition, $\mathrm{Tr}(\rho) = 1$, which ensures normalization. Pure states also fulfill $\mathrm{Tr}(\rho^2) = 1$, while for mixed states $\mathrm{Tr}(\rho^2) < 1$. An important example for mixed states is the completely depolarized state

$$\begin{pmatrix} 1/2 & 0 \\ 0 & 1/2 \end{pmatrix}, \tag{2.5}$$

which can only be written as sum of pure states $(|0\rangle\langle 0| + |1\rangle\langle 1|)/2$. An intuitive way to represent pure as well as mixed qubit states by means of the Bloch sphere presented in the next section.

2.1.2 Bloch sphere

Any qubit state defined by Eq. (2.2) can be represented visually making use of the Bloch sphere concept [21]. The surface of the sphere displays the two-dimensional parameter space of an arbitrary pure qubit state using the fact that the two parameters θ and ϕ are bounded. Since θ defines to what extent a qubit state is in the $|0\rangle$ - state or $|1\rangle$ - state with values between $[0, \pi]$ it is used as polar angle. The relative qubit phase φ ranges between $[0, 2\pi]$ and is thus displayed via the azimuthal angle. In Fig. 2.1, the Bloch sphere is shown with a Bloch vector representing a pure qubit state indicated by a red arrow. Any point on the surface of the sphere corresponds to a pure qubit state and vice versa.

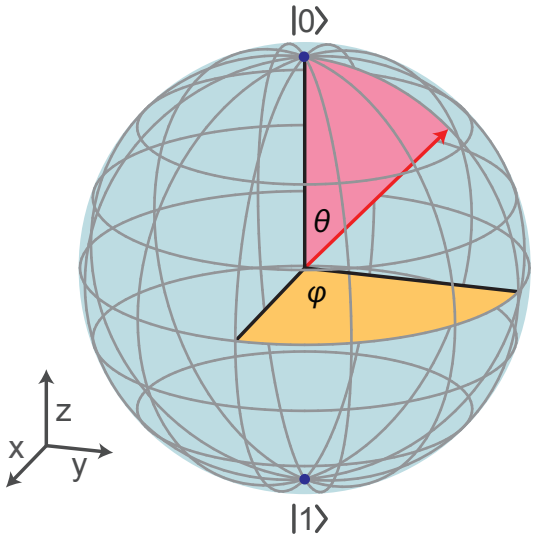

Figure 2.1: Bloch Sphere representation. The Bloch vector (red) indicates a pure quantum state defined by angles θ and φ as described in Eq. (2.2).

The representation of a qubit state using a Bloch vector is not restricted to pure states. An arbitrary qubit state defined by a density matrix ρ in Eq. (2.4) can be converted into a Bloch vector and vice versa using the following formula [21]

$$\rho = \frac{1}{2}\left(\mathbb{I} + \boldsymbol{\sigma} \cdot \boldsymbol{a}\right) = \frac{1}{2}\begin{pmatrix} 1 + a_z & a_x - ia_y \\ a_x + ia_y & 1 - a_z \end{pmatrix} \tag{2.6}$$

where $\boldsymbol{\sigma} = (\sigma_x, \sigma_y, \sigma_z)$ is the vector of Pauli matrices defined as

$$\sigma_x \equiv \begin{pmatrix} 0 & 1 \\ 1 & 0 \end{pmatrix} \qquad \sigma_y \equiv \begin{pmatrix} 0 & -i \\ i & 0 \end{pmatrix} \qquad \sigma_z \equiv \begin{pmatrix} 1 & 0 \\ 0 & -1 \end{pmatrix} \tag{2.7}$$

The formulas above are valid for both, mixed states and pure states. For mixed qubit states the Bloch vector does not point on the surface but inside the sphere. As an example, the origin of the Bloch sphere with coordinates $(0, 0, 0)^T$ belongs to the completely depolarized state described by Eq. (2.5).

Experimentalist convention In real-world physics, the two qubit states $|0\rangle$ and $|1\rangle$ are encoded in a system with two distinguishable energy levels. The lower energy level is referred to as $|g\rangle$ - state since a quantum system without external stimulation resides in the "ground" state. When exciting the qubit, it populates the $|e\rangle$ - state which is referred to as "excited" state. Experimental physicists consider the z-axis

of the Bloch sphere as energy scale and thus label the southern pole as $|g\rangle$ - state and the northern pole as $|e\rangle$ - state. This results in the following relabeling

$$|0\rangle \leftrightarrow |e\rangle \qquad\qquad |1\rangle \leftrightarrow |g\rangle \tag{2.8}$$

We will need the experimental physics convention when introducing our transmon qubit in Sec. 2.2.3.

2.1.3 Quantum gates

Gates are necessary for any computing logic. In order to manipulate classical bit states, gates are applied. A classical gate is defined by a mapping of the two possible initial states onto well-defined target states using a 2x2 lookup table. One example is the NOT gate, which inverses the bit.
Similar to classical logic gates, qubit gates allow a mapping between initial and target states. In contrast to classical gates, this mapping has to be unitary, i.e., each inital state on the Bloch sphere has a unique mapping to a final state, which is also on the Bloch sphere. Nonunitary mappings imply a loss of quantum information. Due to the two continuous degrees of freedom determining a single qubit state, an infinite number of gates is possible. In fact, any rotation of a Bloch vector can be viewed as a visual representation of a qubit gate. Rotations about an arbitrary axis $\boldsymbol{n} = (n_x\ n_y\ n_z)^T$ are described by the following formula [21]

$$\hat{R}_{\boldsymbol{n}}(\alpha) = e^{-i\frac{\alpha}{2}\boldsymbol{n}\cdot\boldsymbol{\sigma}} = \cos\frac{\alpha}{2}\mathbb{1} - i\sin\frac{\alpha}{2}\boldsymbol{n}\cdot\boldsymbol{\sigma} \tag{2.9}$$

where α is the angle of rotation and $\boldsymbol{\sigma}$ the vector of Pauli matrices described by Eq. (2.7). For rotations about the x, y or z axis we obtain

$$\hat{R}_x(\alpha) = \begin{pmatrix} \cos\frac{\alpha}{2} & -i\sin\frac{\alpha}{2} \\ -i\sin\frac{\alpha}{2} & \cos\frac{\alpha}{2} \end{pmatrix} \quad \hat{R}_y(\alpha) = \begin{pmatrix} \cos\frac{\alpha}{2} & -\sin\frac{\alpha}{2} \\ \sin\frac{\alpha}{2} & \cos\frac{\alpha}{2} \end{pmatrix} \quad \hat{R}_z(\alpha) = \begin{pmatrix} e^{-i\frac{\alpha}{2}} & 0 \\ 0 & e^{i\frac{\alpha}{2}} \end{pmatrix}, \tag{2.10}$$

where, in our experiment, we are especially interested in the $\hat{R}_y^\pi$-gate, performing a rotation of an angle π about the y-axis of the Bloch sphere.

$$\hat{R}_y^\pi = \begin{pmatrix} 0 & -1 \\ 1 & 0 \end{pmatrix} \tag{2.11}$$

It effectively maps the $|1\rangle$ - state to the $|0\rangle$ - state and vice versa.

In order to perform quantum computation based on this theory, we need a physical device providing us with a two-level system in the quantum regime. The next section gives some insight in our implementation based on superconducting quantum circuits.

2.2 Superconducting quantum circuits

For enabling experiments with qubits, various quantum resources have been established. The approach we focus on in this thesis is to use superconductivity as macroscopic quantum resource. In contrast to earlier approaches using ions or single atoms, superconducting quantum circuits fulfil crucial requirements such as scaling. One drawback are the low temperatures necessary to ensure superconductivity.

2.2.1 Macroscopic quantum model

The macroscopic quantum model allows to phenomenologically describe the phenomenon of superconductivity [22]. It describes an ensemble of highly correlated superconducting electrons without explaining the microscopic background. The superconducting state and thus all highly correlated electrons are described by a wave function

$$\Psi(\boldsymbol{r}, t) = \Psi_0 e^{i\theta(\boldsymbol{r},t)}, \tag{2.12}$$

where Ψ_0 is the amplitude and $\theta(\boldsymbol{r}, t)$ is the phase. The squared absolute value of the wave function can be viewed as the density of superelectrons in our system. The description of superconductivity as macroscopic quantum effect is the foundation of using superconducting devices for quantum computing. It leads to a quantum treatment of Josephson junctions, which results in a nonlinear inductance described in the next section.

2.2.2 Josephson inductance

A Josephson tunnel junction consists of an insulating barrier between two superconducting electrodes [23]. Up to some critical current I_c, the junction is capable of transporting a tunneling supercurrent across the non-superconducting interface. The junction behavior can be desribed using the Josephson equations which give rise to various physical phenomena [23, 24]. We are interested in the nonlinear

inductance of a Josephson junction described by [22]

$$L_\mathrm{J} = \Phi_0/(2\pi I_\mathrm{c} \cos\varphi), \tag{2.13}$$

where $\Phi_0 = 2 \times 10^{15}$ Vs is the magnetic flux quantum. The Josephson inductance depends on the phase difference φ between the two macroscopic wave functions Ψ_1 and Ψ_2 describing the superconducting state in the junction electrodes. It is nonlinear in the variable φ and can even become negative. For suitable junction parameters, the phase φ can be treated as quantum variable [25].
In the next section, we explain the effect of exchanging the linear inductance of a quantum harmonic oscillator with the nonlinear inductance of a Josephson junction in the quantum regime. As we will se, the nonlinearity enables us to implement an artificial two-level system using the lowest two energy levels.

2.2.3 Transmon qubit

The qubit design used in our experiment is the nowadays state of the art transmon qubit for solid state quantum computing [26]. Transmon qubits originate from the cooper pair box (CPB) [27] by adding an additional shunt capacitance [28]. This results in an exponentially decreased charge noise sensitivity but has the drawback of a reduced anharmonicity. Anyway, the transmon qubit design offers coherence times exceeding 100 μs and is therefore used in scaled quantum computing architectures with multiple qubits [8].
The transmon qubit is explained best by comparing it to a quantum harmonic oscillator [29]. In Fig. 2.2 (b), the transmon qubit circuit is shown. It differs from the quantum harmonic oscillator circuit from Fig. 2.2 (a) by replacing the linear inductive element with a Josephson junction. As described in Sec. 2.2.2, the junction possesses a non-linear inductance which causes deviations from the equidistant energy level spacing. Provided the junction is fabricated to operate in the quantum regime, the overall circuit Hamiltonian of a transmon qubit can be written as [28]

$$\mathcal{H}_\mathrm{q} = 4E_\mathrm{C}(\hat{N} - N_\mathrm{g})^2 - E_\mathrm{J}\cos\hat{\varphi}, \tag{2.14}$$

where $E_\mathrm{C} = e^2/(2C_\Sigma)$ is the charging energy and $E_\mathrm{J} = I_\mathrm{c}\Phi_0/2\pi$ the Josephson energy with I_c being the critical current of the junction. The overall junction capacitance $C_\Sigma = C_\mathrm{J} + C_\mathrm{S}$ can be tuned by engineering the shunt capacitance C_S, allowing to design $E_\mathrm{J}/E_\mathrm{C} \approx 50$ which is a good compromise between charge noise insensitivity and sufficient residual anharmonicity [28]. In Eq. (2.14), the electron number $\hat{N}$ and

the phase $\hat{\varphi}$ act as conjugate quantum variables. Using a perturbative approach, the eigenenergies of the transmon qubit in the limit $E_J/E_C \gg 1$ can be expressed as [28]

$$E_m = -E_J + \sqrt{8E_C E_J}\,(m + 1/2) - \frac{E_C}{12}\left(6m^2 + 6m + 3\right), \tag{2.15}$$

where m labels the energy levels. Using Eq. (2.15), we can calculate the energy of the three lowest energy levels. The anharmonicity between the energy differences $E_1 - E_0$ and $E_2 - E_1$ is $\alpha \approx -E_C/\hbar$.

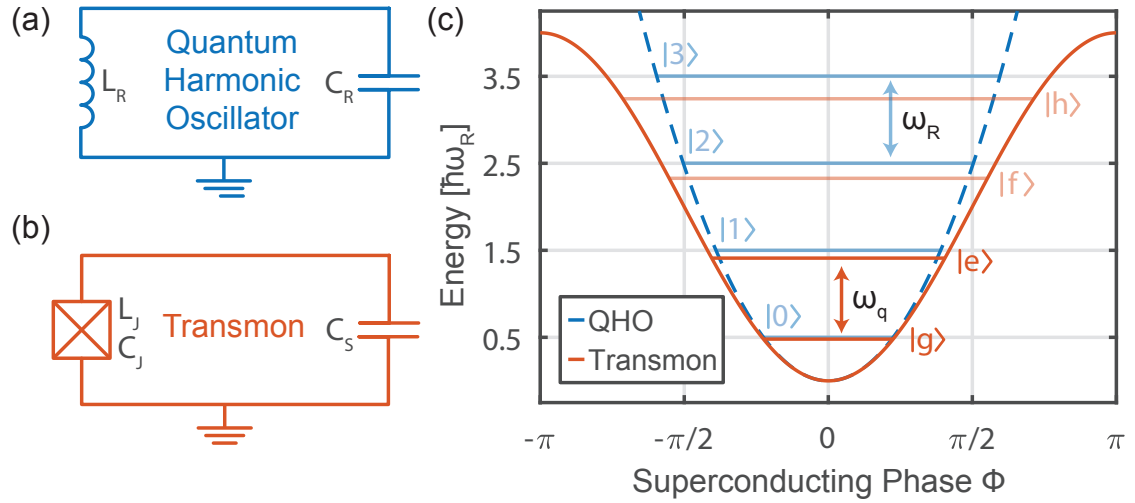

Figure 2.2: (a) Quantum harmonic oscillator (QHO) circuit diagram with inductance L_R and capacitance C_R, (b) Transmon qubit circuit consisting of Josephson junction (crossed box) with capacitance C_J and inductance L_J shunted with capacitance C_S. (c) Transmon qubit and QHO energy level scheme with highlighted qubit levels $|e\rangle$ and $|g\rangle$.

In Fig. 2.2 (c), the energy level structure of a transmon qubit compared to the equidistant energy level structure of a quantum harmonic oscillator is shown. The eigenstates corresponding to the energy levels described by Eq. (2.15) are labeled as $|g\rangle$, $|e\rangle$, $|f\rangle$ and $|h\rangle$ with their eigenenergies rising from $|g\rangle$ to $|h\rangle$. The anharmonicity of the transmon qubit level structure allows us to selectively address the lowest two energy levels as artificial quantum two-level system. Thus, the transmon qubit Hamiltonian can equivalently be expressed as

$$\mathcal{H}_q = \frac{\hbar}{2}\omega_q \hat{\sigma}_z, \tag{2.16}$$

where $\omega_q = (E_1 - E_0)/\hbar$. In Eq. (2.16), higher transmon qubit levels are omitted as indicated in Fig. 2.2 (c). The simplification in Eq. (2.16) is insufficient for practical

qubit operation, since the low anharmonicity of a transmon qubit leads to state leakage to higher levels for short drive signals [30, 31]. This effect puts a lower limit to the gate time of a transmon qubit.
Any transmon qubit needs to be read out at some point during quantum information processing tasks. A widespread method to do so is to couple the transmon qubit to a superconducting resonator which is then probed [32]. Our memory sample uses the multimode structure of a 3D-cavity described in the next subsection.

2.2.4 3D-cavity resonator

The idea behind using a 3D-cavity as resonator coupled to a transmon qubit is to make use of the multimode structure defined by the cavity geometry [9, 10]. The first two modes couple roughly equally strong to the qubit, but the second mode is decoupled from the antennas used for control and readout. In this way one can use the cavity for both, storage and readout purposes. The boundary conditions for the electric or magnetic field in a rectangular cavity allows for the following TEM modes with frequencies [33]

$$\nu_{mnl} = \frac{c}{2\pi\sqrt{\mu_\mathrm{r}\epsilon_\mathrm{r}}}\sqrt{\left(\frac{m\pi}{a}\right)^2 + \left(\frac{n\pi}{b}\right)^2 + \left(\frac{l\pi}{d}\right)^2}, \tag{2.17}$$

where c is the speed of light, μ_r the relative permeability and ϵ_r the relative permittivity. The dimensions of the rectangular cavity, $a \times b \times d$, spatially restrict the modes of the electric field and result in the discretization shown in Eq. 2.17. For a detailed drawing of the cavity, we refer to Ref. [9].
Each mode is described by the textbook Hamiltonian for the quantum harmonic oscillator [21]

$$\mathcal{H}_\mathrm{osc} = \hbar\omega_\mathrm{r}\left(\hat{a}^\dagger\hat{a} + 1/2\right), \tag{2.18}$$

where ω_r is the eigenfrequency of the resonator and $\hat{a}^\dagger$ ($\hat{a}$) the photon creation (annihilation) operator, respectively. Adapting Eq. (2.18) to the 3D-cavity needs to take care of any possible mode and reads

$$\mathcal{H}_\mathrm{cav} = \hbar\sum_{m,n,l}\omega_{mnl}\left(\hat{a}^\dagger_{mnl}\hat{a}_{mnl} + 1/2\right) = \hbar\sum_{m,n,l}\omega_{mnl}\left(\hat{n}_{nml} + 1/2\right), \tag{2.19}$$

where $\omega_{mnl} = 2\pi\nu_{mnl}$ are the possible modes described by Eq. (2.17). The creation ($\hat{a}^\dagger_{mnl}$) and annihilation ($\hat{a}_{mnl}$) operators are adding or removing a photon with frequency ω_{mnl} from the cavity mode. Eigenstates of the Hamiltonian in Eq. (2.19)

are so-called Fock states

$$\hat{a}^{\dagger}_{nml}\hat{a}_{mnl}\left|n_{mnl}\right\rangle = n_{nml}\left|n_{mnl}\right\rangle, \tag{2.20}$$

where n_{mnl} is the number of photons stored the resonator mode with frequency ω_{mnl}. As we will see in the next subsection, the coupling between qubit and a resonator described by Eq. (2.19) leads to phenomena enabling us to store and to readout qubit states.

2.3 Qubit-resonator coupling

The transmon qubit and the 3D-cavity resonator are coupled via the engineered dipole moment of the transmon qubit circuit [9, 10]. This enables the two devices to exchange energy quanta. In our case of strong coupling, this can be done coherently multiple times before the excitation is lost to the environment [32].

2.3.1 Jaynes-Cummings Hamiltonian

For strong coupling, the coupling strength g needs to be higher than the actual qubit and cavity decay rates $\kappa, \gamma \ll g$. Furthermore, the coupling strength needs to be much smaller than the eigenfrequencies of the system $\omega_{\mathrm{q}}, \omega_{\mathrm{c}} \gg g$. In the case of strong coupling, the interaction between qubit and a single resonator mode can be well described using the Jaynes-Cummings Hamiltonian [29, 32]

$$\begin{aligned}\mathcal{H}_{\mathrm{JC}} &= \mathcal{H}_{\mathrm{q}} + \mathcal{H}_{\mathrm{cav}} + \mathcal{H}_{\mathrm{coupling}} && (2.21)\\ &= \frac{\hbar\omega_{\mathrm{q}}}{2}\hat{\sigma}_z + \hbar\omega_{\mathrm{c}}\left(\hat{a}^{\dagger}\hat{a} + 1/2\right) + \hbar g\left(\hat{\sigma}^{+}\hat{a} + \hat{\sigma}^{-}\hat{a}^{\dagger}\right), && (2.22)\end{aligned}$$

where the coupling term describes the coherent excitation transfer from qubit to cavity mode ($\hat{\sigma}^{+}\hat{a}$) and vice versa ($\hat{\sigma}^{-}\hat{a}^{\dagger}$). Our coupled qubit-cavity system is designed to operate in the dispersive regime, where the qubit transition frequency ω_{q} and the cavity mode resonance frequency ω_{c} are detuned by an amount of $\Delta \equiv \omega_{\mathrm{q}} - \omega_{\mathrm{c}}$. Provided the detuning is larger than the coupling strength, $\Delta \gg g$, we can make use of the interaction picture and expand the Hamiltonian in Eq. (2.22) up to second order. This leads to the following, easier accessible representation [32]

$$\mathcal{H}_{\mathrm{disp}}/\hbar = \frac{1}{2}(\omega_{\mathrm{q}} + \chi)\hat{\sigma}_z + (\omega_{\mathrm{c}} + \chi\hat{\sigma}_z)\hat{a}^{\dagger}\hat{a}, \tag{2.23}$$

where $\chi = g^2/\Delta$. The Hamiltonian in Eq. (2.23) can be solved analytically, exhibiting new eigenstates [32]. In Fig. 2.3 (a) and Fig. 2.3 (b), the energy level structure for the uncoupled qubit-cavity system as well as for the coupled qubit-cavity system are shown, respectively.

Regarding Eq. (2.23), the qubit transition frequency and the cavity mode resonance frequency are shifted compared to the uncoupled case. These shifts can be viewed in Fig. 2.3 (b). The qubit transition frequency is increased by an amount of χ which is referred to as the Lamb shift. For the cavity mode, the resonance frequency is also altered by an amount of χ referred to as AC Stark shift. It is either decreased if the qubit is in ground state or increased if the qubit is in excited state.

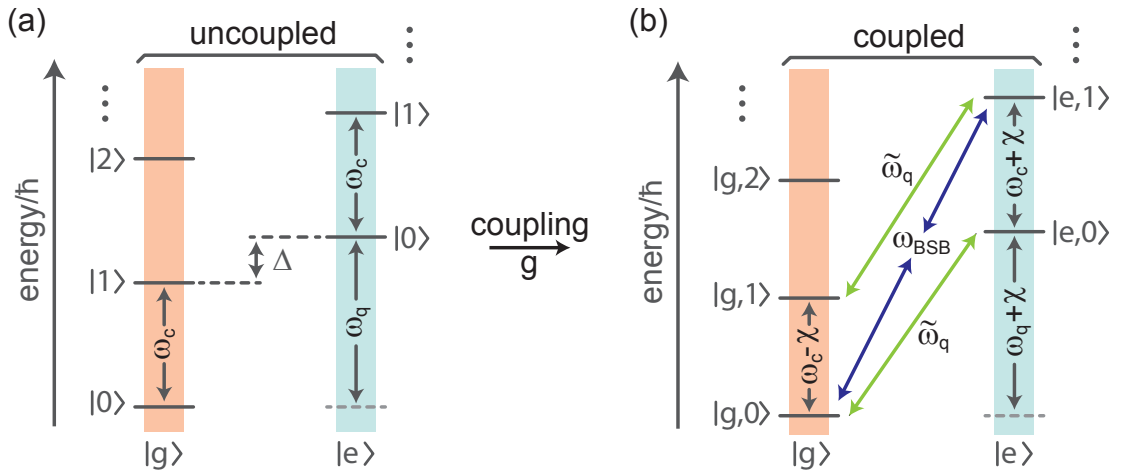

Figure 2.3: In (a) the energy level scheme of an uncoupled qubit-cavity system with corresponding qubit and resonator transition energy is shown. Including a finite coupling g leads to the altered level scheme shown in (b). Energy levels in the blue region correspond to resonator ket states with excited qubit whilst levels in the orange region correspond to resonator ket states with qubit in the ground state. Transitions necessary for this thesis are indicated by arrows.

2.3.2 Blue sideband transition

When regarding Fig. 2.3 (b), other transitions than the regular qubit $|g,0\rangle$ to $|e,0\rangle$ transition can be driven. The transition from the $|g,0\rangle$ state to the $|e,1\rangle$ state indicated by the blue arrows is called blue sideband (BSB) and is of high importance for our quantum memory implementation. By taking the sum of qubit and cavity transition energy, the blue sideband is defined as

$$\omega_{\mathrm{BSB}} = \tilde{\omega}_{\mathrm{q}} + \tilde{\omega}_{\mathrm{c}} \tag{2.24}$$

where $\tilde{\omega}_q$ and $\tilde{\omega}_c$ are the shifted qubit transition and mode resonance frequencies as discussed in the following section.
The blue sideband transition excites the qubit whilst also creating a single photon fock state in our resonator. Due to selection rules, a direct transition between the energy level of the $|g,0\rangle$ state and $|e,1\rangle$ state is forbidden [34–37]. Thus, a two-photon process driven at half the transition frequency is necessary.
Together with the $|g,1\rangle$ to $|e,1\rangle$ qubit transition, the blue sideband transition allows to store an arbitrary qubit state encoded in a resonator fock state [11]. A requirement for using the $|g,1\rangle$ - state as memory for qubit states is a long lifetime of the resonator mode which is achieved by using a mode that is almost decoupled from the cavity antenna (cf. Sec. 3.1.1 and Fig. 3.2). The lifetime of the transferred qubit state is thus not limited by the qubit lifetime (cf. Sec. 2.4.2) buth rather by the lifetime of this so-called "memory" mode [10].

2.3.3 Coupling-induced frequency shifts

Dispersive shift for readout

Another possibility that arises from the coupling between qubit and cavity is to read out the state of the qubit. It can be directly seen in Eq. (2.23) that the qubit state alters the resonance frequency of a coupled mode by $\pm\chi$ depending on whether the qubit is in ground or in excited state. In Fig. 2.4, the phase and magnitude response of a resonator mode for a coupled qubit in ground and in excited state is shown. By probing the resonator mode at a fixed frequency, one can detect the state of the qubit. This kind of measurement is called dispersive readout [32]. It allows to measure the z-projection of our quantum state continuously in time. In our experiment, we use the phase since it shifts almost linear in a regime close to the resonance frequency.
A requirement for using a coupled cavity mode for readout purposes is a fast decay of the mode. This is achieved by using a mode that exhibits considerable coupling

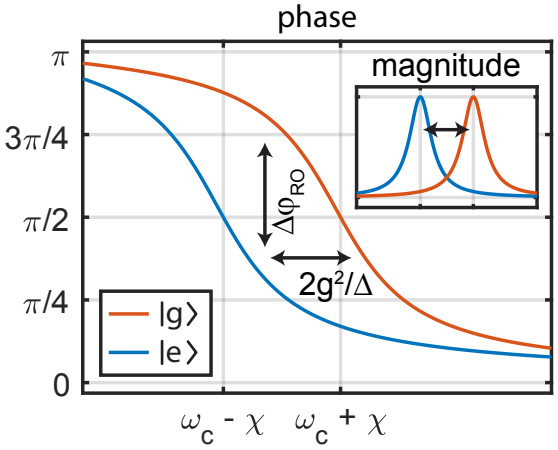

Figure 2.4: Resonator response for qubit in excited and ground state, respectively.

to the cavity antenna (cf. Sec. 3.1.1 and Fig. 3.2). This "readout" mode needs to decay significantly faster than the qubit.

Transmon qubit dispersive shift

The dispersive shift of a transmon qubit is not only affected by the transition between ground and excited state. It is necessary to include the parasitic $|e\rangle$ to $|f\rangle$ transition. With the third level included, the effective dispersive shift is defined as [28]

$$\chi' = \chi_{01} - \frac{\chi_{12}}{2} \tag{2.25}$$

where χ_{01} is the dispersive shift induced by the qubit transition and χ_{12} the dispersive shift induced by the $|e\rangle$ to $|f\rangle$ transition. Due to the higher coupling to the parasitic transition, even negative effective dispersive shifts are possible. The overall readout mode resonance frequency depending on the qubit state is finally defined as

$$\tilde{\omega}_\mathrm{r} = \omega_\mathrm{r} - \frac{\chi_{12}}{2} + \chi'\hat{\sigma}_z. \tag{2.26}$$

Thus, the effective dispersive shift χ' is not relative to the bare resonator frequency ω_r but to a shifted frequency $\omega_\mathrm{r} - \chi_{12}/2$. Applying Eq. (2.26) to ground and excited state of the qubit leads to the following altered readout mode resonance frequencies depending on the qubit state

$$|g\rangle \rightarrow \tilde{\omega}_\mathrm{r} = \omega_\mathrm{r} - \chi_{01} \qquad |e\rangle \rightarrow \tilde{\omega}_\mathrm{r} = \omega_\mathrm{r} + \chi_{01} - \chi_{12}, \tag{2.27}$$

where the difference equals $2\chi'$. Using a more sophisticated approach including any higher transmon qubit levels, the altered dispersive shift in Eq. (2.25) can be expressed as [28]

$$\chi' = \frac{g^2}{\Delta}\frac{\alpha}{\Delta + \alpha} \tag{2.28}$$

where g is the coupling strength, Δ the detuning between qubit and resonator and α the anharmonicity of the transmon qubit. The term g^2/Δ can be identified as the bare shift χ_{01} induced by the qubit transition.

Stark shift

In quantum mechanics, the dispersive shift χ' is a two-way effect. By rearranging Eq. (2.23), we can get an expression for the altered qubit resonance frequency

$$\tilde{\omega}_\mathrm{q} = \omega_\mathrm{q} + 2n\chi' + \chi', \tag{2.29}$$

where $n = \langle \hat{a}^\dagger \hat{a} \rangle$ is the number of photon excitations in the coupled mode. Thus, for an increasing number of photons we get an increasing shift of our qubit transition frequency.
To summarize, describing the coupling between qubit and resonator using the Jaynes Cummings model leads to interesting quantum phenomena. Solving it leads to new eigenstates, a new energy level structure and to a dependence between the qubit state and the resonance frequency of a coupled mode. In the next subsection, we continue our description of superconducting quantum circuits by explaining the dynamics of driven quantum two-level system.

2.4 Qubit dynamics

In equilibrium, the qubit will always stay in the ground state if thermal excitations are neglected or negligible. Using well-controlled drive pulses, other energy levels as indicated by the energy level scheme in Fig. 2.3 (a) can be populated. This dynamic property of the qubit is the basis for the implementation of qubit gates.

2.4.1 Rabi theory

An electric field that couples to the dipole moment of the transmon qubit circuit effectively acts as rotating drive in x-y plane regarding the Bloch sphere picture. Both, qubit and driving field, are thus described by the driven qubit Hamiltonian [38]

$$\mathcal{H}_\mathrm{Rabi} = \mathcal{H}_\mathrm{q} + \mathcal{H}_\mathrm{drive} \tag{2.30}$$

$$= \frac{\hbar\omega_\mathrm{q}}{2}\hat{\sigma}_z + \frac{\hbar\Omega_\mathrm{d}}{2}\left(\hat{\sigma}_- e^{+i\omega_\mathrm{d}t+i\varphi_\mathrm{d}} + \hat{\sigma}_+ e^{-i\omega_\mathrm{d}t-i\varphi_\mathrm{d}}\right), \tag{2.31}$$

where Ω_d is the drive power which is proportional to the amplitude of the electric drive field, ω_d is the drive frequency and φ_d the drive phase. Here, we have approximated the sinusoidal with a rotating drive. Solving the Hamiltonian is possible by

using a rotating frame transformation [32]. The transformed Hamiltonian can be written as

$$\mathcal{H}_{\mathrm{Rabi}} = \frac{\hbar}{2}\left[\Delta\omega\hat{\sigma}_z + \Omega_{\mathrm{d}}(\hat{\sigma}_x\cos\varphi_{\mathrm{d}} + \hat{\sigma}_y\sin\varphi_{\mathrm{d}})\right] \tag{2.32}$$

$$\Delta\omega = \omega_{\mathrm{q}} - \omega_{\mathrm{d}} \tag{2.33}$$

where the drive field has a fixed direction in the x-y plane specified by the phase φ_{d} of the drive. The solution of this Hamiltonian in the case of no detuning $\Delta\omega = 0$ and phase zero $\varphi_{\mathrm{d}} = 0$ is

$$|\Psi(t)\rangle = \cos\frac{\Omega_{\mathrm{d}}t}{2}|g\rangle + i\sin\frac{\Omega_{\mathrm{d}}t}{2}|e\rangle\,. \tag{2.34}$$

The effect of the drive field can thus be viewed as rotation on the Bloch sphere depending on the duration of the drive pulse. The expectation value of the $|e\rangle$-level population can be calculated via projection on the wave function $P_{\mathrm{e}} = |\langle e|\Psi(t)\rangle|^2$ and leads to

$$P_{\mathrm{e}} = \frac{\Omega_{\mathrm{d}}^2}{\Delta\omega^2 + \Omega_{\mathrm{d}}^2}\sin^2\left(\frac{t\sqrt{\Delta\omega^2 + \Omega_{\mathrm{d}}^2}}{2}\right), \tag{2.35}$$

where the projected wavefunction $|\Psi(t)\rangle$ is an extended version of Eq. (2.34) including a finite detuning $\Delta\omega$. The prefactor in Eq. (2.35) effectively reduces the highest possible expectation value of the excited state. We can attribute this effect to a tilted rotation axis depending on the detuning $\Delta\omega$ [9].

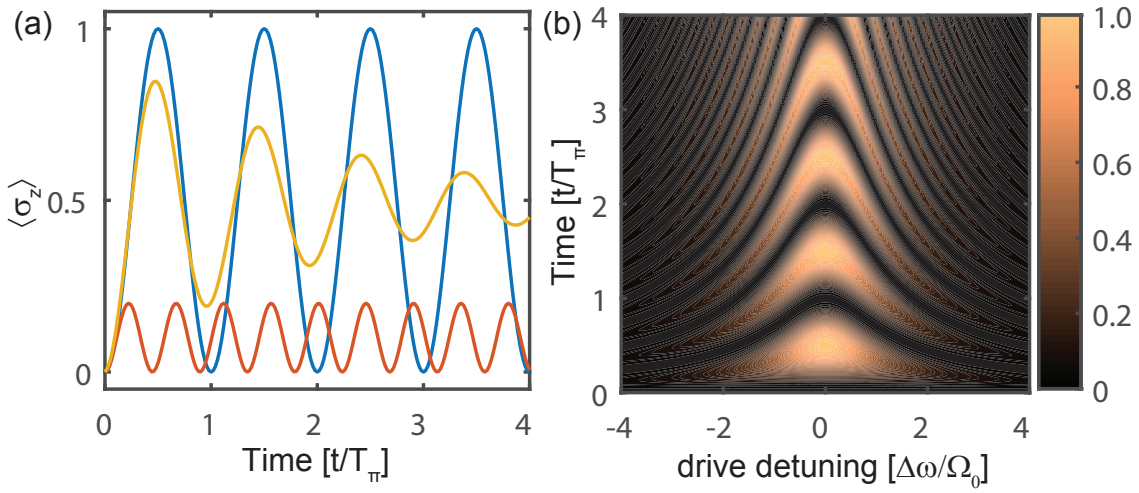

Figure 2.5: (a) Rabi traces. Blue: resonant drive without decay. Yellow: resonant drive with decay. Red: detuned drive with $\Delta\omega/\Omega_{\mathrm{d}} = 2$. (b) Rabi traces mapped versus drive detuning $\Delta\omega/\Omega_{\mathrm{d}}$.

Motivated by Eq. (2.35), drive pulses can give acces to quantum state manipulation by precisely adjusting the pulse duration and pulse phase. Thus the polar angle can be rotated by a desired amount specified by the pulse duration among an axis specified by the phase φ_d of the drive signal. Together with virtual z-rotations enabled by adjusting the phase [39], this represents a set of universal single-qubit gates.
We map Eq. (2.35) in Fig. 2.5 (b) for varying detuning and pulse duration. With increasing detuning, the peak value of the amplitude decreases and the Rabi frequency which is given by $\Omega_\mathrm{R} = \sqrt{\Delta\omega^2 + \Omega_\mathrm{d}^2}$ increases. In Fig. 2.5 (a), the blue and the red curve show time traces of resonant and detuned driven qubits, respectively. The yellow curve refers to the real-world scenario, where coupling to environment leads to decoherence, forcing the Bloch vector to collapse to the center of the Bloch sphere (cf. Sec. 2.4.2).

2.4.2 Quantifying decoherence

In circuit quantum electrodynamics, devices exhibit coupling to their environment leading to a loss of quantum coherence [29, 40]. In many cases, those processes can be phenomenologically described by an exponential decay following two different timescales.

1. T_1 decay which forces the qubit z-projection to decay from the excited state to the ground state by transferring energy to the environment.

2. T_φ decay which causes the phase variable of the qubit defined by φ in Eq. (2.2) to dephase, i.e. be indefinable.

T_φ is referred to as pure dephasing time. Whilst the T_1 decay time can be measured directly, the dephasing time T_φ is inaccessible by measurement. Instead, the T_2 decay time can be used as a measure for dephasing. It is linked to the pure dephasing time T_φ and the pure energy decay time T_1 via the following formula

$$\frac{1}{T_2} = \frac{1}{2T_1} + \frac{1}{T_\varphi}. \tag{2.36}$$

For determining the bare T_1 or T_2 decay times, specific protocols exist. The pulse schemes defining those measurement protocols are shown in Fig. 2.6 (d)-(f). In Fig. 2.6 (a)-(c) the qubit state evolution is visualized when applying those protocols.

T_1 Measuring the T_1-time is done by preparing the qubit in the $|e\rangle$ - state and projecting it after some evolution time Δt. The exponantial decay curve depending on the evolution time gives access to the energy decay. The protocol for measuring the T_1-time is shown in Fig. 2.6 (d).

T_2 The T_2-time can be measured using two different protocols. The Ramsey protocol takes the qubit initially to a superposition state with expectation value $\langle\hat{\sigma}_z\rangle = 0$ and defined qubit phase φ which lies in the equatorial plane of the Bloch sphere as indicated in Fig. 2.6 (b). After some free evolution time Δt the qubit state is rotated back from the equatorial plane to the perpendicular plane and then measured. With increasing free precession time, the dephasing increases and the outcome of the measurement approaches a completely depolarized state with expectation value $\langle\hat{\sigma}_z\rangle = 0$.

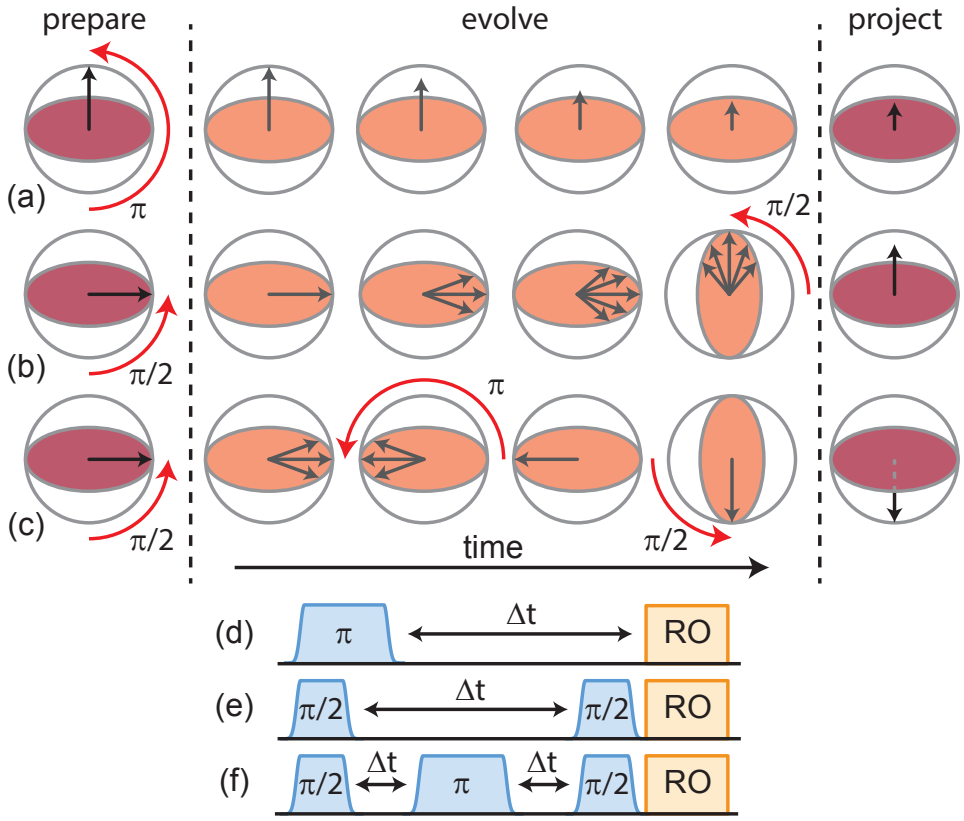

Figure 2.6: Different pulse protocols shown as Bloch Sphere picture (a)-(c) and as pulse schemes (e)-(f). Subfigure (a) and (d) depict the T_1 decay measurement, (b) and (e) the Ramsey protocol for T_2^* decay, (c) and (f) the Hahn echo protocol for $T_{2\mathrm{E}}$ decay, respectively.

Another possibility to measure the T_2-time is the Hahn echo (spin echo) protocol

shown in Fig. 2.6 (f), which effectively is a modified Ramsey protocol with a π-pulse in between forcing coherent dephasing to refocus again [41]. Spin echo and Ramsey protocols can be viewed as different filtering functions for the environment [42]. Hence, they provide information on the nature of the environment. To distinguish between the two protocols, we denote the Ramsey time T_2^* and the Hahn echo time $T_{2\mathrm{E}}$.
The measurements described in this section give direct access to the coherence properties of our qubits. More sophisticated measurement techniques quantifying prepared states and gate qualities are described in the next section.

2.5 Quantum measurements

2.5.1 Quantum state tomography

Quantum state tomography (QST) is an experimental technique to determine the Bloch vector of a prepared single qubit quantum state. In quantum mechanics, measurements only reveal a part of the information which is encoded in the quantum state. In our case, the only accessible axis for measurements is the z-axis. We can detect in which amount the qubit is in the $|e\rangle$ or in the $|g\rangle$ state without knowing the qubit phase. Thus, our measurement projects the qubit to the z-axis by averaging over many measurements (cf. Sec. 2.3.3).
For a detailed reconstruction of the quantum state, each dimension of the Bloch vector needs to be projected. This makes QST a projective measurement of the quantum state. Each Bloch vector dimension is mapped individually giving access to full information about the quantum state. The protocol of quantum state tomography is defined by three steps

1. Measure z-axis projection (a_z)
2. Measure x-axis projection (a_x)
3. Measure y-axis projection (a_y)

The x and y axis projection is done by rotating the qubit by an angle of $\pi/2$ previously among an axis defined by the phase of the drive signal. In Fig. 2.7 the pulse protocols of the three relevant measurements for determining the quantum state are shown.

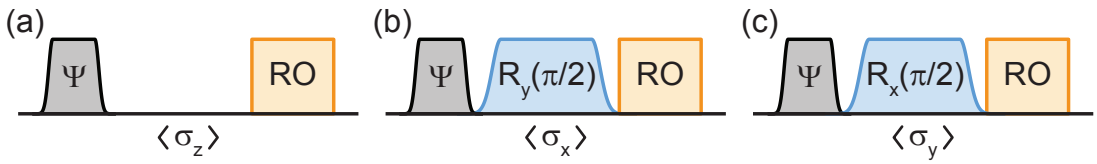

Figure 2.7: Quantum state tomography pulse protocols. In (b) and (c) the qubit state Ψ prepared by the initial pulsescheme is rotated about the y-axis (b) or the x-axis (c) by an angle of $\pi/2$ before readout.

With Eq. (2.6), the measured Bloch vector components a_z, a_x and a_y can be used to reconstruct the density matrix of the initially prepared quantum state. In our experiment, we perform each projection multiple times in order to get precise results. One drawback of QST is the necessity of an ideal $\pi/2$ pulse needed for rotations together with a well-calibrated measurement setup allowing to control the phase precisely. Imperfect pulses used in the pulse protocols shown in Fig. 2.7 lead to distorted reconstructions.

2.5.2 Quantum process tomography

Quantum Process Tomography (QPT) is a useful tool for quantifying the fidelity of quantum operations. Here we give a short introduction for QPT on quantum two-level systems. Detailed information on QPT in general can be found in Refs. [21, 43]. To motivate the derivation of QPT, we start by defining quantum operations described as superoperator $\mathcal{E}(\hat{\rho})$ acting on density matrices. This operator effectively maps an initial quantum state $\hat{\rho}$ to a final state $\hat{\rho}'$. We can express this quantum operation using trace-preserving Kraus operators $\hat{E}_i$ and write it as decomposed operator sum [44]

$$\mathcal{E}(\hat{\rho}) = \sum_{i=1}^{4} \hat{E}_i \hat{\rho} \hat{E}_i^{\dagger}. \tag{2.37}$$

Since we lack information on our Kraus operators, we can choose a fixed operator basis $\{\hat{B}_m\}$ and again rewrite Eq. (2.37) to

$$\mathcal{E}(\hat{\rho}) = \sum_{m,n=1}^{4} \hat{B}_m \hat{\rho} \hat{B}_n^{\dagger} \chi_{mn} \tag{2.38}$$

where χ is the positive and Hermitian quantum process matrix obtained by reshaping χ_{mn} in a (4×4) matrix. By choosing the fixed operator basis $\{\hat{B}_m\}$ we swap the information about our unknown superoperator $\mathcal{E}$ from the Kraus operators $\hat{E}_i$ to the process matrix χ. To get some insight in our quantum process we have to

experimentally determine the process matrix. We do so by applying our quantum process to a set of four independent quantum states $\{\hat{\rho}_i\}$ of our system. The initial density matrices $\hat{\rho}_i$ are basis states spanning our (2×2) qubit state space. The outcome of an applied quantum process on our initial states $\hat{\rho}_i$ can then be decomposed in the $\hat{\rho}_i$-basis

$$\mathcal{E}(\hat{\rho}_i) = \sum_{j=1}^{4} \lambda_{ij} \hat{\rho}_j \tag{2.39}$$

Inserting Eq. (2.38) into Eq. (2.39) results in a system of equations which can be solved for χ [21]. To summarize, we get experimental access to our hermitian process matrix by measuring the effect of our superoperator $\mathcal{E}$ on our set of independent quantum states $\{\hat{\rho}_i\}$ as described by Eq. (2.39).
In experiment, we proceed by choosing our fixed operator basis to be $\{\mathbb{1}, \hat{\sigma}_x, -i\hat{\sigma}_y, \hat{\sigma}_z\}$. As set of independent initial states we use $\{\hat{\rho}_i\} = \{|g\rangle, |e\rangle, |+\rangle, |-\rangle\}$. We use the two eigenstates, $|g\rangle$ and $|e\rangle$, together with the superposition states $|+\rangle \equiv (|0\rangle + |1\rangle)/\sqrt{2}$ and $|-\rangle \equiv (|0\rangle - |1\rangle)/\sqrt{(2)}$ since they are experimentally easy accessible [45].
For an easier reconstruction of our process matrix χ, we switch to the following basis of auxiliary density matrices which do not represent valid qubit states but form a basis of the (2×2) qubit state space.

$$\hat{\rho}_1 = \begin{pmatrix} 1 & 0 \\ 0 & 0 \end{pmatrix} \quad \hat{\rho}_2 = \begin{pmatrix} 0 & 1 \\ 0 & 0 \end{pmatrix} \quad \hat{\rho}_3 = \begin{pmatrix} 0 & 0 \\ 1 & 0 \end{pmatrix} \quad \hat{\rho}_4 = \begin{pmatrix} 0 & 0 \\ 0 & 1 \end{pmatrix} \tag{2.40}$$

We then calculate the action of our quantum process $\mathcal{E}$ on those states by decomposing them in a sum of our set of actual measured initial states.

$$\hat{\rho}'_1 = \mathcal{E}(|g\rangle\langle g|) \tag{2.41}$$

$$\hat{\rho}'_2 = \mathcal{E}(|+\rangle\langle +|) + i\mathcal{E}(|-\rangle\langle -|) - \frac{1+i}{2}[\mathcal{E}(|g\rangle\langle g|) + \mathcal{E}(|e\rangle\langle e|)] \tag{2.42}$$

$$\hat{\rho}'_3 = \mathcal{E}(|+\rangle\langle +|) - i\mathcal{E}(|-\rangle\langle -|) - \frac{1-i}{2}[\mathcal{E}(|g\rangle\langle g|) + \mathcal{E}(|e\rangle\langle e|)] \tag{2.43}$$

$$\hat{\rho}'_4 = \mathcal{E}(|e\rangle\langle e|) \tag{2.44}$$

Finally, using the linear algebra solution described in [21], we can calculate our process matrix with the following formula

$$\chi = \Lambda \cdot \begin{pmatrix} \hat{\rho}'_1 & \hat{\rho}'_2 \\ \hat{\rho}'_3 & \hat{\rho}'_4 \end{pmatrix} \cdot \Lambda, \qquad \text{where} \qquad \Lambda = \frac{1}{2} \begin{pmatrix} \mathbb{I} & \hat{\sigma}_x \\ \hat{\sigma}_x & -\mathbb{I} \end{pmatrix}. \tag{2.45}$$

The process matrix $\hat{\chi}$ together with our fixed operator basis $\{\hat{B}_m\}$ allows us to calculate the action of our quantum process to any initial state $\hat{\rho}$ by applying Eq. (2.38). We visualize our quantum process in Sec. 4.3 by plotting a Bloch sphere map of final states $\hat{\rho}' = \mathcal{E}(\hat{\rho})$. For extracting Kraus operators, Refs. [9, 18, 21] give a more detailed description of process tomography in general.
An important technical detail of our quantum process tomography is the possibility to obtain unphysical density matrices with $Tr(\hat{\rho}) > 1$ due to measurement artifacts. We solve that problem by using a maximum likelihood approach mapping those states back on the Bloch sphere [18].

2.5.3 Fidelity

We quantify the quality of our quantum gates described as quantum processes by using the fidelity as a measure of similarity between two quantum states [21]

$$\mathcal{F}(\hat{\rho}, \hat{\rho}') = Tr\left[\sqrt{\sqrt{\hat{\rho}'} \cdot \hat{\rho}_t \cdot \sqrt{\hat{\rho}'}}\right], \tag{2.46}$$

where $\hat{\rho}_t$ is the desired final quantum state in theory and $\hat{\rho}'$ is the result of our quantum process. Since the process matrix χ can be viewed as a two-qubit quantum state with $Tr(\chi) < 1$, we can apply Eq. (2.46) to our process matrix [18].

Chapter 3

Methods

3.1 Experimental setup

This section gives a description of our experimental setup. It starts with a brief explanation of our memory sample fabricated by E. Xie [9] in Sec. 3.1.1. In Sec. 3.1.2 and Sec. 3.1.3 the necessary electronics and wiring enabling us to operate our memory sample are shown. We finish the description of our experiment by introducing our time-domain pulseshaping technique in Sec. 3.1.4 followed by our readout scheme shown in Sec. 3.1.5.

3.1.1 Compact 3D quantum memory

Our quantum memory experiment sample consists of a 3D-Cavity made of aluminium with a transmon qubit chip inside [9, 10]. The cavity geometry is designed to exhibit a low quality-factor readout mode and a high quality-factor storage mode.

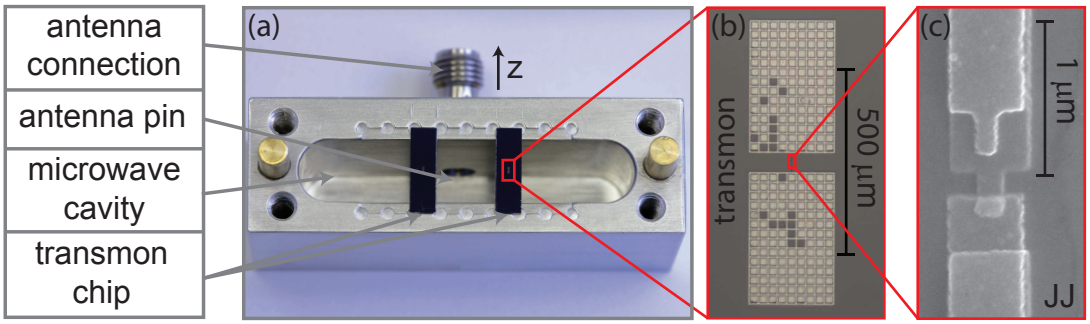

Figure 3.1: (a) 3D cavity half with transmon qubit chip and dummy chip inserted (black rectangles). (b) Optical micrograph of transmon qubit. The rectangular paddles acting as capacitive plate are connected via a Josephson Junction. (c) Scanning electron microscopy image of Josephson junction.

In Fig. 3.1 (a), one half of our cavity with inserted transmon qubit and dummy chip is shown. The modes relevant for our experiment exhibit an electric field in z-direction, the same direction of our transmon qubits dipole moment. Figure 3.1 (b) shows the transmon qubit with its two superconducting paddles made out of aliminium acting as capacitance. The Josephson junction which exhibits the nonlinear inductance necessary to establish an artificial two-level system as described in Sec. 2.2.3 is shown in Fig. 3.1 (c). It is fabricated using shadow evaporation to generate a thin, non-superconducting aluminium oxide layer between two aluminium electrodes [46].

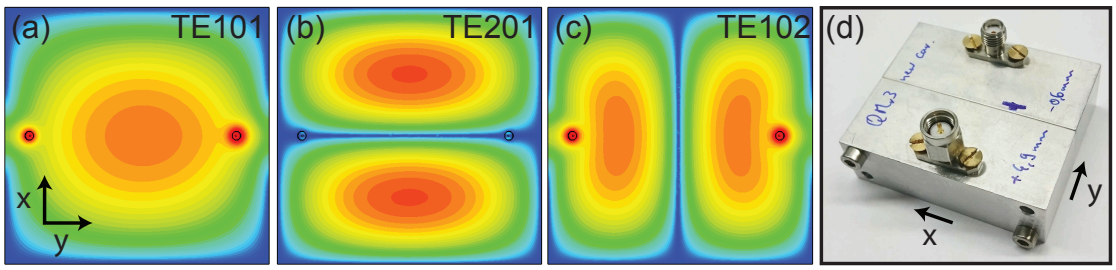

Figure 3.2: Electric field distribution of readout mode (a), storage mode (b) and twin mode (c) in cavity xy-plane. Small circles are in and output antenna ports. Image (d) shows an actual image of the cavity with in- and output antenna.

In Fig. 3.2 (a) to (c) the magnitude of the electric field distribution (Simulation by E. Xie) of the lowest three modes in z-direction is mapped over the x-y plane. The high quality-factor storage mode in (b) has a negligible electric field magnitude at the antenna positions which results in low coupling. The low Q-factor readout mode in (a) has a considerably electric field magnitude close to the antenna which results in losses through the ports. Both modes exhbit coupling of their electric field distributions to the transmon qubit dipole moment whilst the storage twin mode in (c) is designed to decouple from the qubit.

3.1.2 Cryogenic setup

Our quantum memory experiment is embedded in the low temperature stage of a He^3/He^4 dilution refrigerator with a base temperature of approximately 30 mK. A more detailed description of the refrigerator working principles can be found in Refs. [47, 48].

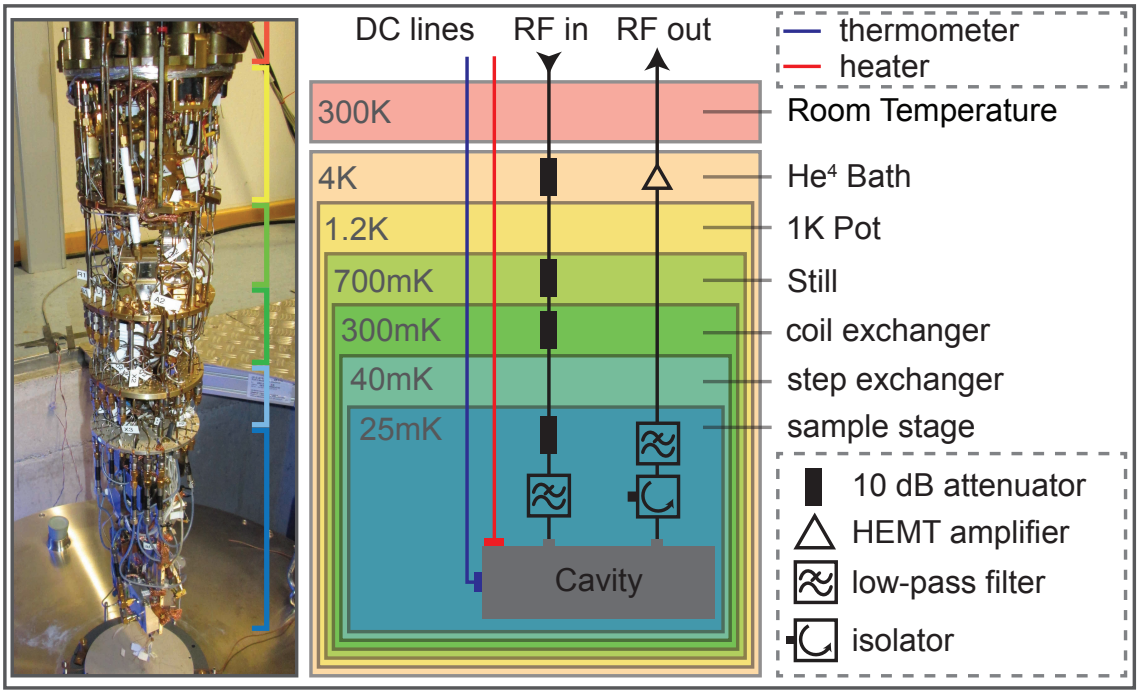

Figure 3.3: Image and schematic drawing of dilution refrigerator low temperature stage embedding our quantum memory experiment.

The low temperature stage shown as image and as schematic drawing in Fig. 3.3 contains our quantum memory experiment denoted as cavity at 30 mK. It is connected via AC wiring for input and output signals at GHz frequencies. As a result of the low power needed for transitions we attenuate our input signal by 40 dB. The output signal leaving the refrigerator needs to be amplified in order to measure at room temperature. This is done at 4 K using a cryogenic HEMT amplifier (+42dB) and again at room temperature using an RF amplifier (+22dB). Both amplifiers add noise to the output signal making the use of an FPGA-enhanced digitizer card for averaging crucial. DC lines connected with a thermometer and a heater allow us to precisely control the sample temperature.

3.1.3 Pulse generation setup

For generating pulsed microwave signals acting as qubit gates (cf. Sec. 2.4.1) we make use of an arbitrary waveform generator (AWG) for pulse shaping. As indicated in Fig. 3.4 we use several identical Agilent 81160A AWGs for that purpose (denoted 81160A in Fig. 3.4). The generated pulse envelopes act as I and Q components (cf. Sec. 3.1.4) used as input for our RF sources.

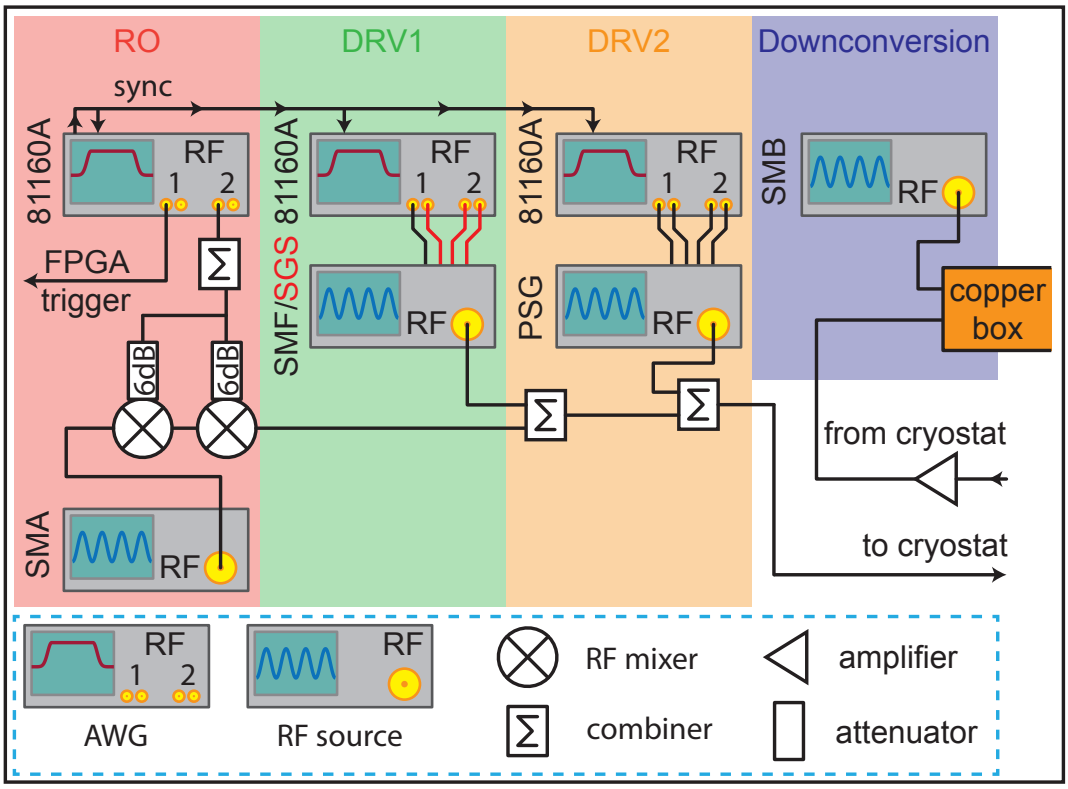

Figure 3.4: Schematic drawing of our pulse generation setup. Three couples of AWG and RF devices allow for generating readout (RO) pulse and two drive pulses (DRV1 & DRV2) with different frequency and power.

The RF sources used in our experiment are of three different types. Most important our Keysight PSG vector signal generator (denoted PSG in Fig. 3.4) which is capable of providing high power microwave pulses whilst offering the option of a differential wideband IQ input. The wideband IQ input with a range of 800 MHz offers smooth modulation. In conclusion the PSG RF source is the most reliable one.
The second RF source used in our experiment is the R&S SMF100A microwave signal generator (denoted SMF in Fig. 3.4) which has a good on/off ratio but no

wideband IQ input. It can only be operated in pulsed mode. Throughout this thesis it showed problems at providing stable high-power pulselength sweeps.
The third RF source available is the R&S SGS100A RF source (denoted SGS in Fig. 3.4). It offers pulse modulation via wideband IQ inputs. The drawback of the SGS100A is the instability in the high power regime necessary for the BSB pulse together with signal leakage occuring at lower power.
For readout purposes, we downconvert the signal emerging the cryostat using a R&S SMB100A microwave signal generator (denoted SMB in Fig. 3.4) acting as local oscillator. The downconversion is done inside a shielded copper box (cf. Sec. 3.1.5). In order to have phase stability at GHz frequencies the devices have to be synchronized. We do so by connecting all our devices to a 10 MHz rubidium atomic reference clock.

3.1.4 Pulseshapes and IQ-modulation

For defining our pulseshapes with specific length, phase and shape we make use of the IQ-decomposition of a microwave signal using the following formula

$$\begin{aligned} S(t) &= A(t)\sin(\omega t + \varphi) \\ &= I\sin\omega t + Q\cos\omega t \end{aligned} \tag{3.1}$$

where $I = A(t)\cos\varphi$ and $Q = A(t)\sin\varphi$ are the in-phase and quadrature variables of the drive signal. Using an Agilent81160A arbitrary waveform generator (AWG), the I and Q components of a microwave signal can be defined on a nanosecond timescale. In experiment, it turns out that a flat-top Gaussian shape reduces state leakage due to avoiding a sharp transition. The flat-top pulse consists of a rising and falling slope with a constant part in between. In Fig. 3.5, a typical flat-top Gaussian pulse is plotted with a ramp time t_{ramp} of 20 ns. We use this ramp time throughout the whole experiment since it is a good tradeoff between shortness demanded for applicable gates and length demanded for harmonic gates. The formula describing the shape

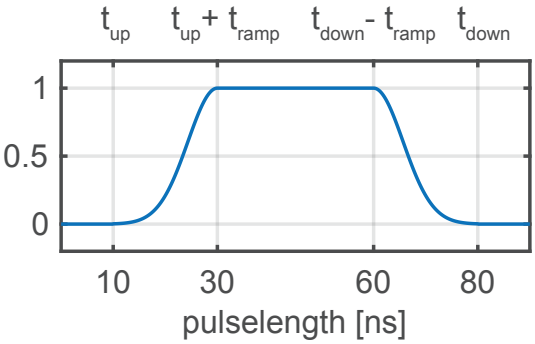

Figure 3.5: Flat-top Gaussian pulse.

is defined as

$$A(t) = \begin{cases} \exp\left[-\left(\frac{t/t_{\text{ramp}}-1}{2\sigma}\right)^2\right] & \text{if } t_{\text{up}} < t < t_{\text{up}} + t_{\text{ramp}} \\ 1 & \text{if } t_{\text{up}} + t_{\text{ramp}} < t < t_{\text{down}} - t_{\text{ramp}} \\ \exp\left[-\left(\frac{t/t_{\text{ramp}}}{2\sigma}\right)^2\right] & \text{if } t_{\text{down}} - t_{\text{ramp}} < t < t_{\text{down}} \end{cases} \tag{3.2}$$

where t_{up} defines the starting time of the pulse, t_{down} the end and t_{ramp} the duration of the slope in nanoseconds as indicated in Fig. 3.5. The variable σ defines the shape of the slope and has a value of $\sigma = 0.2$. Equation (3.2) does not match with the standard Gaussian nomenclature but effectively is of the same shape. The difference is due to the easier implementation in LabView.

Using the pulse shaping of the I and Q component on a nanosecond timescale described above we are able to modify a simple RF signal with fixed frequency and fixed power. In our experiment we use the differential IQ inputs of our R&S PSG Vector Network Analyzer to modulate our carrier signal. As described in Eq. (3.1), a time dependent I and Q component of our AWG output results in a time dependent Amplitude $A(t)$ and phase φ of our RF pulse.

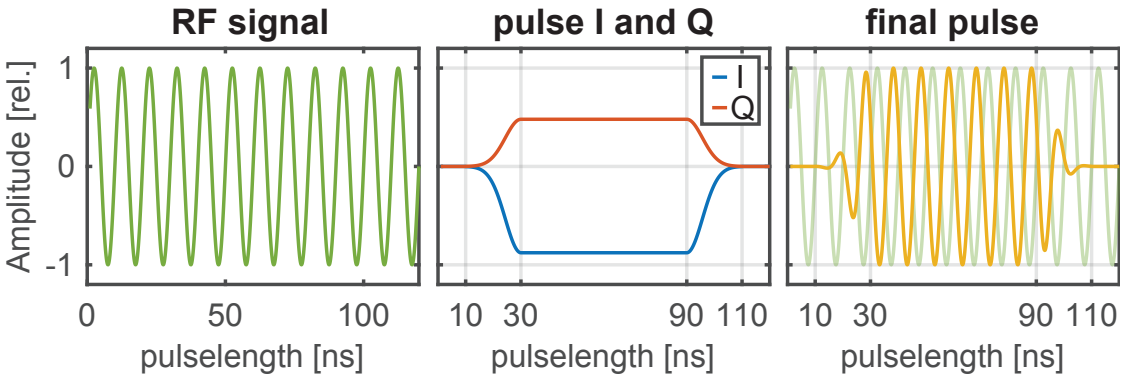

Figure 3.6: Left: continuous signal from RF source without IQ modulation. Middle: pulse I and Q components as specified by our "Deepthought" measurement program. Right: Final pulse after pulse modulation.

In Fig. 3.6, the result of a pulse modulation with our flat-top Gaussian pulse defined by Eq. (3.2) is shown. The phase of the resulting signal is controlled by the ratio of the in-phase and quadrature component $\varphi = \arctan(Q/I)$ which is highlighted in the final pulse sequence (right).

3.1.5 Time domain readout with FPGA

In Sec. 2.3, we described the dispersive shift as an effect that shifts the resonance frequency of a mode depending on the state of a coupled qubit. Here, we present our technical solution enabling us to detect that shift.

Our time domain readout setup shown in Fig. 3.4 sends a readout pulse at a probing frequency close to the readout mode resonance frequency. When leaving the cryostat, the readout signal needs to be amplified which is adding a lot of noise exceeding the signal by at least one order of magnitude [47]. This makes averaging crucial.

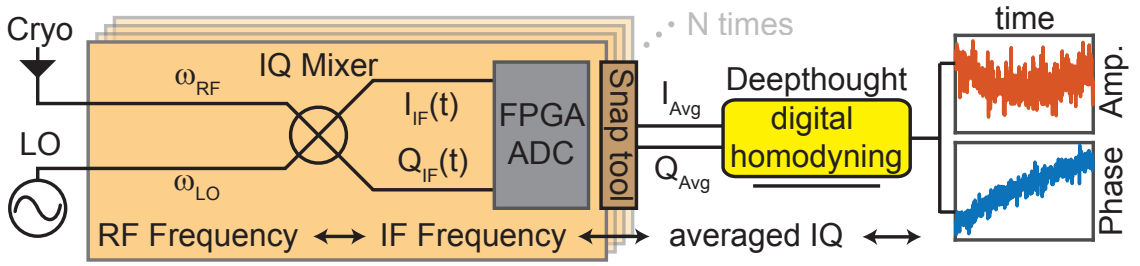

Figure 3.7: Simplified readout scheme with downconversion in copper box (orange rectangle) and digital homodyning ("Deepthought" program). More details can be found in Refs. [9, 47].

As indicated in Fig. 3.7, the amplified signal emerging the cryostat is mixed with an IQ mixer separating it into I and Q components at an intermediate frequency of 62.5 MHz. The downconversion is done inside a shielded copper box. Analog components of the downconversion setup are not shown for simplicity.

The I and Q components of the signal at intermediate frequency are then sampled at 512 points via the FPGA card with a sampling rate of 240 MHz and sent to the computer. This scheme is repeated N times for averaging which is done using a C+ code called "Snap tool" (in experiment N $\approx 10^4$ to 10^5). The averaged I and Q components of the signal at intermediate frequency (indicated in Fig. 3.7 as I_{Avg} and Q_{Avg}) are then converted to I and Q DC signals using digital homodyning in our "Deepthought" LabView code. We then extract the phase and amplitude of the readout signal from the time dependent I and Q DC values using an optimization scheme to correct for various deviations [47]. The phase and amplitude curves in the right panel of Fig. 3.7 contain 512 values sampled at a frequency of 240 MHz, which results in a recording time of approximately 2.13 μs. If desired, the FPGA sampling rate can be decreased for achieving a longer readout time. Since the phase response of a mode at resonance changes almost linearly for small deviations it can be regarded as rescaled z-projection of the qubit state. We will refer to this quantity

as readout phase during this thesis.

3.2 Sample characterization

Here we present our results on sample characterization measurements. We do so in order to compare them with the previously measured data by E. Xie [9]. A detailed comparison of the values is given in Tab. 3.1.

3.2.1 Qubit

We start our characterization with a qubit frequency sweep in Fig. 3.8. The circles representing the readout phase are measured following a 200 ns drive pulse with varying frequency. It exhibits the known Rabi pattern shown in Fig. 2.5 (b) for a fixed pulselength. We use Eq. (2.35) as a fit model and initialize all parameters close to the experimental values in order to extract the qubit transition frequency ω_q.

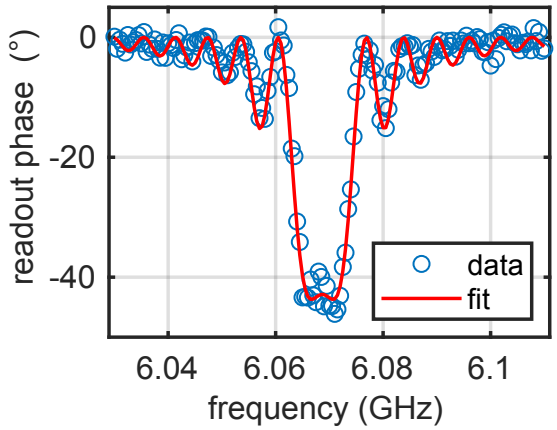

Figure 3.8: Blue circles represent the readout phase measured following a drive pulse with varying frequency close to the qubit transition frequency. The drive power and the pulselength are fixed at -40 dBm and 200 ns, respectively. The red curve represents a fit corresponding to Eq. (2.35) resulting in a qubit transition frequency of 6.0687 GHz.

The fit in Fig. 3.8 reveals a qubit transition frequency ω_q of 6.0687 GHz. The experimental drive pulse length of 200 ns with slopes (cf. Sec. 3.1.4) results in an effective pulselength of approximately 176 ns obtained by fit. Our drive power of 10^{-4} mW (-40dBm) corresponds to a drive frequency Ω_d of 7.9 MHz. The fit also allows us to determine the maximum dispersive phase shift, corresponding to the qubit state in $|e\rangle$, to be approximately 49°.

We continue our sample characterization by measuring the qubit response to a varying pulselength. The qubit exhibits Rabi oscillations (cf. Sec. 2.4.1) which increase their oscillation frequency with increasing drive power. In Fig. 3.9 (a) a map showing the readout phase in dependence of the applied pulse power and the pulselength is shown. We use the Rabi oscillation frequency to determine the conversion factor between the drive power shown at the signal source and the drive frequency in the Hamiltonian in Fig. 3.9 (b). The relation between the two quantities is linear as expected from Eq. (2.35). The slope gives $\Omega_\mathrm{d}\ (\mathrm{MHz}) = 5.07\sqrt{\mathrm{P(mW)}}$. Our fit value obtained from our qubit frequency sweep in Fig. 3.8 corresponds well with the fitted power to frequency conversion.

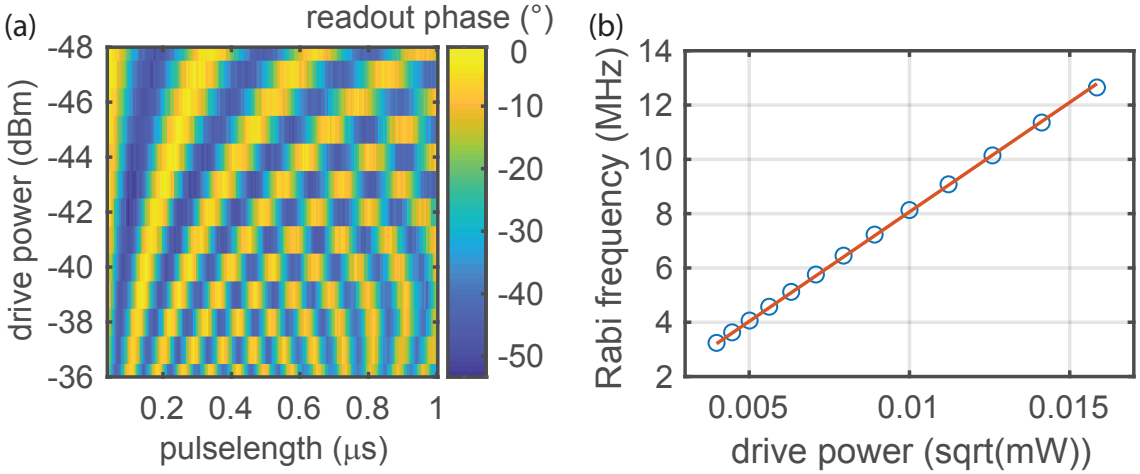

Figure 3.9: In (a), the measured readout phase following a drive pulse at qubit transition frequency with varying power and pulselength is mapped. In (b), the blue circles represent the Rabi frequency for varying drive power. The red line represents a linear fit with a slope of $\Omega_\mathrm{d}(\mathrm{MHz}) = 5.07\sqrt{\mathrm{P(mW)}}$.

Using the basic pulse protocols described in Sec. 2.4.2 allows us to determine the characteristic timescales for qubit decay and qubit dephasing. In Fig. 3.10, prototypical traces for the three protocols discussed in Sec. 2.4.2 and corresponding fits are plotted.

The T_1-time of our qubit is measured using multiple π pulses with increasing free evolution time between pulse and readout. Fitting the exponential decay in Fig. 3.10 (T_1) results in a T_1-time of 1.875 μs. The T_2^*-time measurement in Fig. 3.10 (T_2^*) exhibits its characteristic oscillating behavior due to the weakly detuned drive which allows the Bloch vector representing the quantum state to rotate in the x-y plane. Our exponential sinusoidal fit leads to a T_2^*-time of 1.875 μs.

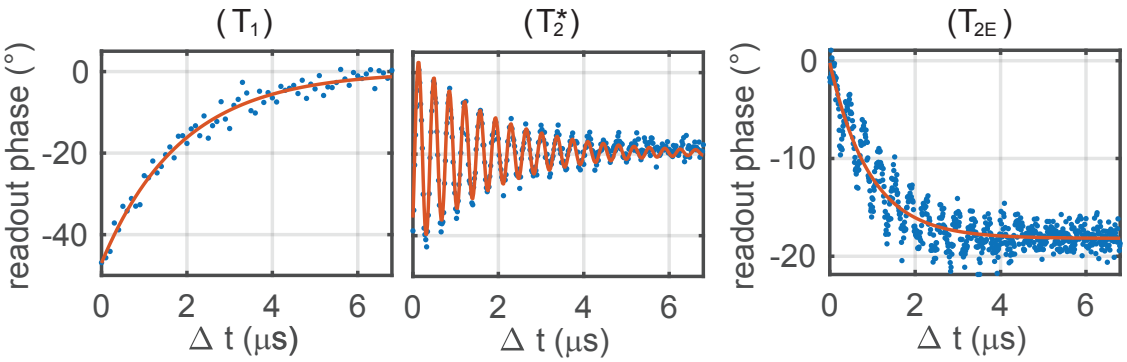

Figure 3.10: Qubit decoherence measurements. In all subfigures, blue data points represent the measured readout phase versus varying free evolution time when applying the protocols shown in Fig. 2.6 (d)-(f). In (T_1), the exponential decay fit reveals a T_1-time of 1.875 μs. The Ramsey measurement in (T_2^*) is fitted using an exponential sinusoidal decay revealing a T_2^*-time of 1.875 μs. In (T_{2E}), the exponential decay fit reveals a decay time of 0.9295 μs resulting in a Hahn echo time of $T_{2E} = 1.939$ μs (cf. Fig. 2.6 (f)).

Using the Spin Hahn protocol with the result shown in Fig. 3.10 (T_{2E}) leads to a T_{2E}-time of 1.939 μs. To prevent confusion we note that the fit value obtained by the exponential decay in Fig. 3.10 (T_{2E}) only gives acces to the free evolution time Δt. In order to obtain the full T_{2E}-time we have to account twice for that time and need to add the π-pulse length of (80 ns) in between too, as specified in the Hahn echo protocol in Fig. 2.6 (f). These times still indicate a significant dephasing caused by low-frequency noise [42].

The curves in Fig. 3.10 represent single measurements, which are known to fluctuate over time. For a precise specification, sufficient statistics would be necessary. Anyway, the shown measurements can be regarded as approximate values since we do not expect the deviation from the distribution mean to be large.

3.2.2 Readout mode

Our time domain setup allows us to measure the resonance curve of the readout mode without using a vector network analyzer (VNA). This kind of measurement is more time consuming and inaccurate than the transmission measurement using a VNA. Anyway, it is sufficient and allows us to measure without changing our setup shown in Fig. 3.4.

We characterize our readout mode by applying a readout pulse only and start measuring after waiting long enough for the photon population in the resonator to be

in equilibrium. Using our FPGA-enhanced digitizer card described in Sec. 3.1.5 we are able to determine the amplitude of the reflected readout signal. This kind of measurement yields the Lorentzian shaped response curves in Fig. 3.11. The measurement thus acts similar to a VNA transmission measurement.

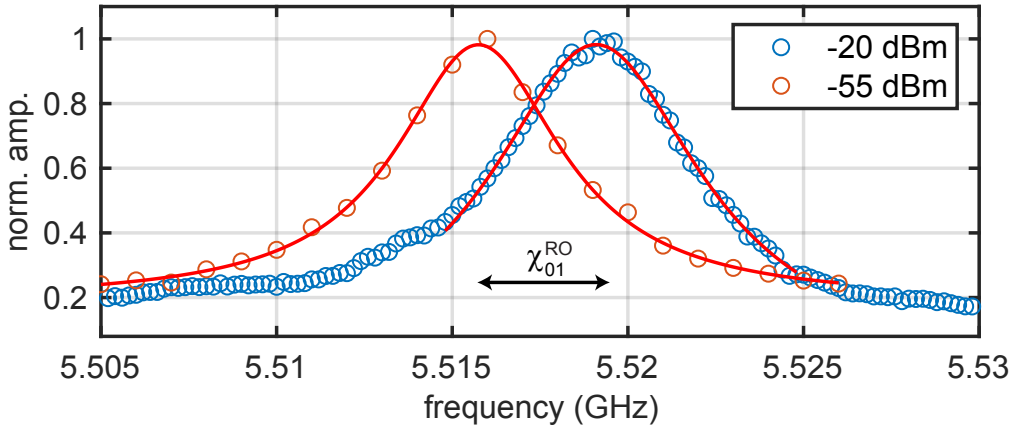

Figure 3.11: Readout mode transmission measuremement. Circles represent the normalized amplitude of the reflected signal for varying drive frequency close to the readout mode resonance. It is measured using the FPGA-enhanced digitizer card. The red curves are obtained by fitting the resonance curves with a regular Lorentzian. The curves shift by an amount of $\chi_{01}^{\mathrm{RO}} = 3.3$ Mhz.

In Fig. 3.11, such a measurement mapping the readout mode is shown. We measure the two curves using two different readout pulse power levels. The curve measured with -55 dBm drive power represented by orange circles leaves the transmon qubit transitions unaffected and can be regarded as coupled readout mode resonance frequency for the transmon qubit in $|g\rangle$ - state described in Eq. (2.27). The blue circles in Fig. 3.12 represent the measurement at a considerably high power of -20 dBm. At this power level, the number of photons in the resonator exceeds a critical number leading to a breakdown of the Jaynes-Cummings model. The measured resonance frequency can be then be regarded as bare readout mode resonance frequency ω_{r}. Regarding Eq. (2.27), we can identify the shift in Fig. 3.11 to be $\chi_{01}^{\mathrm{RO}} = 3.3$ MHz. For determining the reduced dispersive shift χ' of our transmon qubit, we use another approach. In Fig. 3.12 (a), the reflected readout signal amplitude recorded is mapped versus varying length of our qubit drive pulse applied in advance. It is clearly visible that for a sufficient pulselength (approximately 75 ns) the readout mode resonance frequency shifts to a lower frequency due to the excitation of the qubit. In Fig. 3.12 (b) the readout mode resonance frequencies for varying pulselengths are plotted. They are obtained by fitting the Lorentzian shaped resonance curves in

Fig. 3.12 (a). The effective dispersive shift obtained by the frequency difference of readout mode resonance frequency with qubit in $|g\rangle$ and $|e\rangle$ state can be viewed as purely induced by the qubit since the excitation of transitions other than the qubit transition are negligiby small.

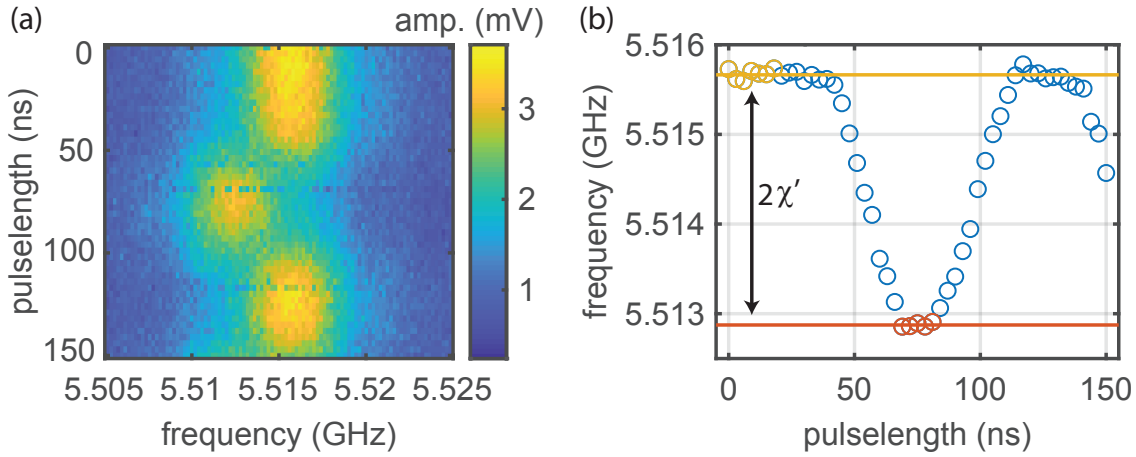

Figure 3.12: (a) Readout mode transmission mapped close to the resonance frequency following a drive pulse at qubit transition frequency with varying pulselength and a fixed drive power of -50 dBm. It is measured using the FPGA-enhanced digitizer card. In (b) the circles represent fitted resonance frequencies of the readout mode for varying pulselength. By averaging the yellow and red colored circles, we estimate the effective dispersive shift of the readout mode to be $\chi'_{\mathrm{RO}} = -1.4$ MHz. The yellow (red) line shows the resonance frequency of the readout mode for qubit in $|g\rangle$-state ($|e\rangle$-state).

Summarizing the measurements above, we determine the dispersive shift to be $\chi' = -1.4$ MHz and the shift between the bare resonator frequency and the qubit in ground state to be $\chi_{01}^{\mathrm{RO}} = 3.3$ MHz. Using Eq. (2.25) we can now identify our shift induced by the third level to be $\chi_{12}^{\mathrm{RO}} = 9.4$ MHz. With χ_{01}^{RO} and Δ at hand, we can finally calculate the coupling coefficient g in Eq. (2.22) describing the interaction strength between qubit and coupled readout mode to be $g = 43$ MHz.

3.2.3 Storage mode

In contrast to the readout mode measurements in Sec. 3.2.2, the frequency sweeps mapping our storage mode transmission are obtained using a vector network analyzer (VNA). Similar to Fig. 3.11 we measure two different curves for high and low VNA power. We do so in order to measure both, the bare resonance frequency of the storage mode and the resonance frequency of the mode for the qubit in ground

state. The result is shown in Fig. 3.13. We determine the shift in resonance to be $\chi_{01}^{S} = -1.33$ MHz and the uncoupled storage mode resonance frequency to be 8.706839 GHz.

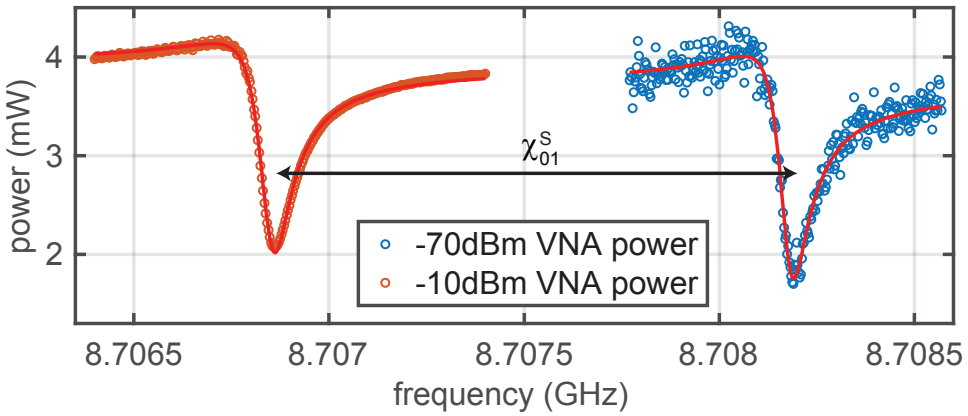

Figure 3.13: Circles represent the reflected power when measuring the storage mode transmission close to resonance with a VNA. Using a modified Lorentzian accounting for cross-coupling between the two resonator ports according to Refs. [49] to fit our transmission curves, we obtain an effective dispersive shift of $\chi_{01}^{S} = -1.33$ MHz.

Using Eq. (2.28), we can calculate the reduced dispersive shift χ_S' to be -87 kHz[1]. Thus, the effective shift of the storage mode is significantly decreased. According to Eq. (2.28), the large detuning $\Delta_{q,S}$ of the storage mode is responsible for that effect. As described in Sec. 2.3, other transitions than the regular qubit transition can be driven. The blue sideband (BSB) pulse indicated in Fig. 2.3 excites the qubit and additionally adds one photon excitation in the storage mode. Thus, the BSB pulse can be regarded as transition from $|g, 0\rangle$ to $|e, 1\rangle$.

In Fig. 3.14 (a), the BSB transition is mapped. The plot shows the readout phase for varying drive power and frequency whilst the pulselength is fixed. For increasing drive power, the transition frequency shifts towards lower frequencies. This behavior can be explained taking into account two phenomena. The first one is the decreasing qubit frequency for an increasing number of photon excitations in a coupled mode called Stark shift. It depends linearly on the drive power which is proportional to the number of photons. The second effect causing the blue sideband transition frequency to decrease is the Kerr nonlinearity depending on the squared power applied. The Kerr effect is not of interest for this thesis and we refer the interested reader to [9, 50].

[1] assuming our anharmonicity $\alpha = -187$ MHz measured by E. Xie did not change

In Fig. 3.14 (b), the power dependent transition frequencies obtained by fitting Fig. 3.14 (a) are shown. The red curve is fitted using a second degree polynomial acocunting for both, Kerr and Stark shift, respectively. The yellow line represents the linear contribution caused by the Stark shift described by Eq. 2.29. Using the slope of the linear fit in Fig. 3.14 (b) we determine a power of 72 μW necessary to excite a single photon.

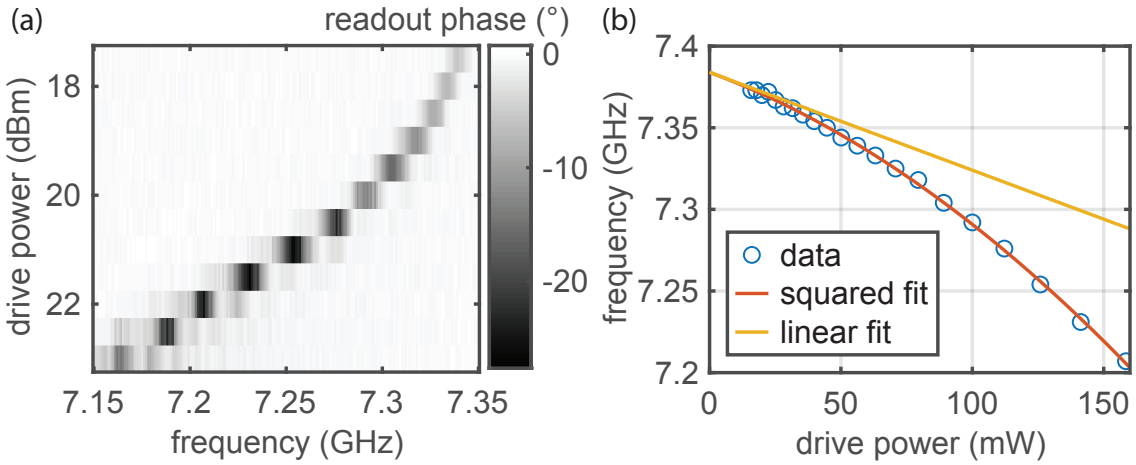

Figure 3.14: (a) Readout phase measured following a drive pulse with a fixed pulse-length of 80 ns mapped for varying drive frequency and power. The power dependent blue sideband transition at frequency ω_{BSB} is clearly visible. In (b) the blue circles represent the BSB transition frequency for varying drive power. We fit the transition frequency with a second degree polynomial (red curve) and obtain a linear contribution caused by the Stark shift (yellow curve) with a fitted slope of -0.6 MHz/mW.

3.2.4 Comparison

In Tab. 3.1, all relevant measured parameters are shown. They summarize the results of our sample characterization measurements in Sec. 3.2. We compare the results with the previously measured values by E. Xie [9].

parameter	Xie 2018	Trattnig 2019
ν_{q} (GHz)	6.234	6.0687
T_1 (μs)	1.3	(1.875 48)
T_2^* (μs)	2.5	(1.875 53)
$T_{2\mathrm{E}}$ (μs)	-	(1.939)
T_φ (μs)	65	-
α (MHz)	-187	-
ν_{RO} (GHz)	5.518	5.519
$\mathrm{FWHM}_{\mathrm{RO}}$ (MHz)	4	5.7[2]
χ'_{RO} (MHz)	-1.4	-1.4
$g_{\mathrm{RO}}/2\pi$ (MHz)	53	43
$\Delta_{\mathrm{q,RO}}/2\pi$ (GHz)	0.716	0.554
ν_{S} (GHz)	8.707546	8.706839
$\mathrm{FWHM}_{\mathrm{S}}$ (kHz)	24.7	102.1
χ'_{S} (kHz)	-77	-93
$g_{\mathrm{S}}/2\pi$ (MHz)	53	59
$\Delta_{q,\mathrm{S}}/2\pi$ (GHz)	-2.474	-2.638

Table 3.1: Sample characterization measurement results compared between Xie (2018) and Trattnig (2019). Values in brackets are not measured using sufficient statistics.

Compared to the values measured by E. Xie, the qubit and storage mode parameters seem to have changed significantly. It is apparent that the decoherence times appear to change massively from cooldown to cooldown. Although T_1 has improved, T_φ has become worse.

[2] might be broadened due to measurement with FPGA

Chapter 4

Experimental results

The experimental results presented here are split into three parts. In the first part presented in Sec. 4.1, we explain our approach for optimizing pulses. In Sec. 4.2 and Sec. 4.3 we present the results of our approach. Finally, in Sec. 4.4 we show our results on measurements where we try to find out why our memory protocol does not work as expected.

4.1 Optimal control engine

In this section we present our "black box" optimization approach to find optimal pulses for our quantum memory experiment. We want to note that our optimal control engine is not directly linked to the mathematical field of optimal control but rather summarizes our efforts towards achieving higher fidelities of quantum gates, including the quantum memory protocol.

4.1.1 CMA-ES

The Covariance Matrix Adaption Evolution Strategy (CMA-ES) is a stochastic method for optimization in non-linear and non-convex search domains. It is a gradient free method which makes it suitable for noisy environments. Our quantum memory takes between 10^4 and 10^5 readout phase averages of the same pulse in order to manage noise contributions in the amplification chain which makes the use of an algorithm which is resiliant to such noise unavoidable.
In general an optimization process can be viewed as a "black box" scenario which aims to minimize an objective function $f(\mathbf{x}) \in \mathbb{R}$ where $\mathbf{x} \in \mathbb{R}^{\lambda}$ represents a point in an n-dimensional search space. The aim of the algorithm is to find the smallest possible $\mathbf{x}'$ in the whole search domain by doing function evaluations as little as

possible. The mechanism behind the objective function $f(\mathbf{x})$ is neither known to the algorithm nor relevant, it is hidden in a "black box".
CMA-ES tracks the function minimization problem by randomly sampling and evaluating possible candidates $\mathbf{x}$ in each optimization step according to a multivariate normal distribution

$$\mathcal{N}(\mathbf{x}|\boldsymbol{\mu}, \boldsymbol{\Sigma}) \sim e^{-\frac{1}{2}(\boldsymbol{x}-\mu)^T \boldsymbol{\Sigma}^{-1}(\boldsymbol{x}-\mu)} \tag{4.1}$$

where the mean $\boldsymbol{\mu}$ and the covariance matrix $\boldsymbol{\Sigma}$ are the parameters defining the distribution.

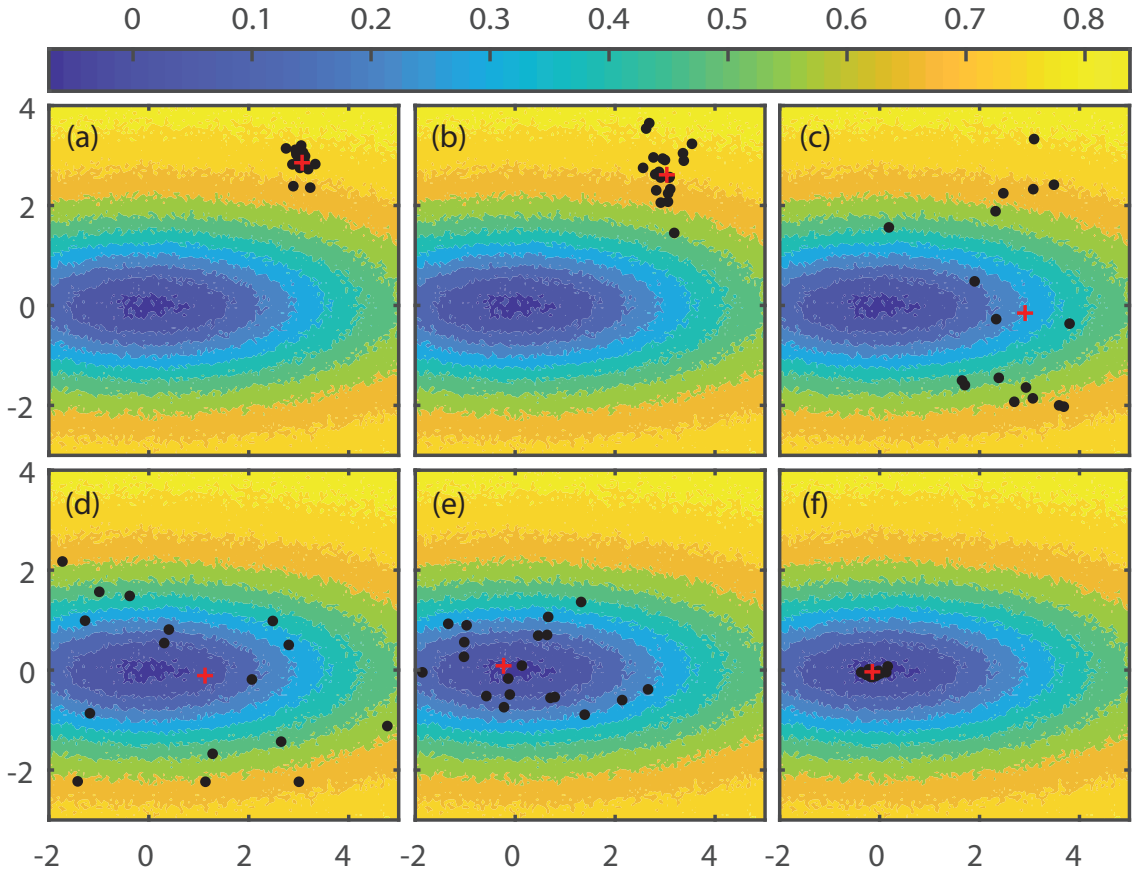

Figure 4.1: CMA-ES optimization on two-dimensional dummy objective function defined in Eq. (4.3). Subfigures (a)-(f) differ in generation number (2,3,6,8,11,25) and show the optimization progress. Red crosses represent the mean of distributions. The 20 black data points in each figure represent candidates within the sampled population.

The optimization steps of an evolutionary algorithm like CMA-ES are called "generations". Each generation consists of λ candidates $\mathbf{x}$ where λ is called "population size". The population size stays constant but candidates are sampled new in every

generation. The mean and the covariance matrix are updated from one generation to another throughout the optimization process. A new generation is sampled according to the following distribution

$$\begin{aligned} \mathbf{x}_k^{(g+1)} &\sim \mathbf{m}^{(g)} + \sigma^{(g)} \mathcal{N}\left(\mathbf{0}, \mathbf{C}^{(g)}\right) \qquad k = 1...\lambda \\ &\sim \mathcal{N}(\mathbf{m}^{(g)}, (\sigma^{(g)})^2 \mathbf{C}^{(g)}) \qquad k = 1...\lambda, \end{aligned} \tag{4.2}$$

where $\mathbf{x}_k^{(g+1)}$ are the new generation candidates. The values determining the distribution for generation $(g+1)$ namely $\mathbf{m}^{(g)}$, $\sigma^{(g)}$, $\mathbf{C}^{(g)}$ are calculated using the knowledge gain from the previously evaluated generations. The covariance of the distribution is given by a product of $\sigma^{(g)}$ and $\mathbf{C}^{(g)}$ where $\mathbf{C}^{(g)}$ is the updated covariance and $\sigma^{(g)}$ is an update factor for the covariance ensuring an increase or decrease if needed and thus ensures a proper movement of the distribution through search space. The calculation of the mean $\mathbf{m}^{(g)}$, the covariance $\mathbf{C}^{(g)}$ and the update factor $\sigma^{(g)}$ is done taking into account information gain from the previously evaluated population of generation (g). Better or worse performing candidates are weighted accordingly resulting in an update which ensures an approach of the mean value $\mathbf{m}$ towards the objective function minimum. Further information for the precise calculation of the updates can be found in Ref. [51].

In Fig. 4.1, an optimization run on a dummy objective function is shown. With increasing generation number, the mean of the distribution moves towards the function minimum at $(0, 0)$. The initial covariance matrix is isotropic with small eigenvalues resulting in a small spread within the 20 sampled candidates. With increasing generation number the spread increases and decreases again after the distribution mean approaches the minimum. It also demonstrates the capability of the CMA-ES algorithm to adapt the covariance matrix for different directions in parameter space accordingly.

The dummy objective function defining the two-dimensional search space in Fig. 4.1 is defined as

$$f(x) = 1 - 10/(0.5x^2 + 4y^2 + 10). \tag{4.3}$$

In order to demonstrate the capability of the CMA-ES algorithm gaussian noise with a standard deviation of 0.02 is added resulting in a noisy landscape.

4.1.2 Optimal control implementation

For optimizing pulse parameters the CMA-ES algorithm described in Sec. 4.1.1 needs to control the relevant pulse parameters. This is enabled using ZeroMQ[1] as messenger. The communication transmits a dictionary

```
comdict = {'search_id': search_id,
           'pulse_id': pulse_id,
           'pulse': pulse,
           'fidelity': 0,
           'do_stop': False}
```

where the `search_id` labels the optimization run and the `pulse_id` defines one specific trasmitted dictionary containing the information of a set of pulse parameters to be evaluated in experiment. The value `pulse` contains another dictionary with pulse parameters.

```
pulse = {'I': I,
         'Q': Q,
         'omega': omega,
         'carrier_amp': carrier_amp}
```

where `I` and `Q` are lists containing I and Q components of the pulseshape in ns resolution, `omega` is the drive frequency and `carrier_amp` the drive power in angular frequency as preferred by theoreticians. The conversion to dBm is done in LabView using the power-dependent Rabi frequency (cf. Fig. 3.9) for calibration.
The overall scheme for optimizing pulses is shown in Fig. 4.2. As indicated, a parameter guess encapsuled in `comdict` is sent to the computer hosting the "Deepthought"-LabView program and evaluated in experiment. After evaluating the single pulse measurement (further data acquisition details can be found in Sec. 3.1), the dictionary `comdict` is changed. The readout phase which acts as fidelity indicator of the experiment is assigned to the key `'fidelity'`. Via the ZeroMQ socket the dictionary `comdict` is sent back to the computer running the python CMA-ES algorithm where it is processed. This cycle of selecting possible candidate parameters by CMA-ES and evaluating them in our experiment takes approximately 5 to 6 seconds and is mainly limited by the averaging and data acquisition on the experimental side.
In order to not confuse the optimizer due to the large differences in orders of magnitude, all parameters are scaled down to a range between 0 and 1 in python. This

[1] https://zeromq.org

ensures stability and equal treatment of each parameter regardless of whether it is large (Frequency - $\mathcal{O}(10^9 s)$) or small (pulselength - $\mathcal{O}(10^{-7} s)$).

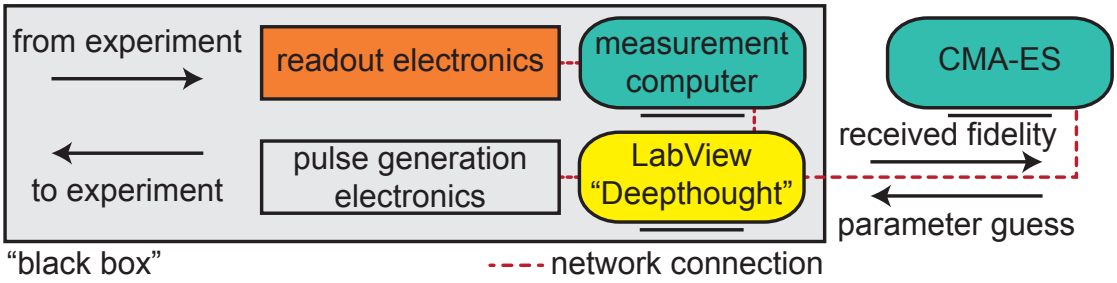

Figure 4.2: Simplified "black box" optimization scheme. Pulse generation electronics controlled via "Deepthought" program (LabView) send pulses to experiment. Measurement computer connected with an FPGA-enhanced digitizer card is measuring and averaging the readout signal, resulting in a detected readout phase processed by "Deepthought". Our CMA-ES optimal control engine is recieving the readout phase as fidelity indicator and sending a new parameter guess.

The protocol which is implemented allows for various pulse implementations. The nanosecond step resolution of the I and Q variables in the communication can be used to perform pulse modulation if the relevant RF source is capable (cf. Sec. 3.1.3). It also offers the opportunity of performing predefined protocols without the use of the "Deepthought" LabView program where protocols have to be defined manually. The implementation in python also gives access to a variety of toolboxes like QuTiP. In our experiment, the PSG vector signal generator was capable of performing frequency modulation which we applied at multiple occasions without recognizing a significant benefit.

4.2 Single pulse optimization

In a first step, we want to optimize π-pulses for the qubit and blue sideband (BSB) transition acting as quantum gates. We do so by applying our optimal control engine to our simple flat-top gaussian pulses (cf. Sec. 3.1.4). For both, qubit and BSB, we used the PSG as RF source which is capable of pulse modulation via wideband IQ inputs (cf. Sec. 3.1.3). The CMA-ES population contained 20 candidates.

4.2.1 Qubit pulse optimization

The qubit π-pulse optimization per hand can be handled quite well. This is due to the stable transition frequency which is independent of the applied power. Thus the mapping of pulselength versus drive power is sufficient for good results. We fix the drive frequency at 6.0687 GHz which is the transition frequency we determined separately (cf. Fig. 3.8), and set the phase of the drive pulse to zero.
In Fig. 4.3, the result of this mapping is shown with our "sweet spot" marked with a red cross in Fig. 4.3 (b). Table 4.1 lists the handoptimized parameters.

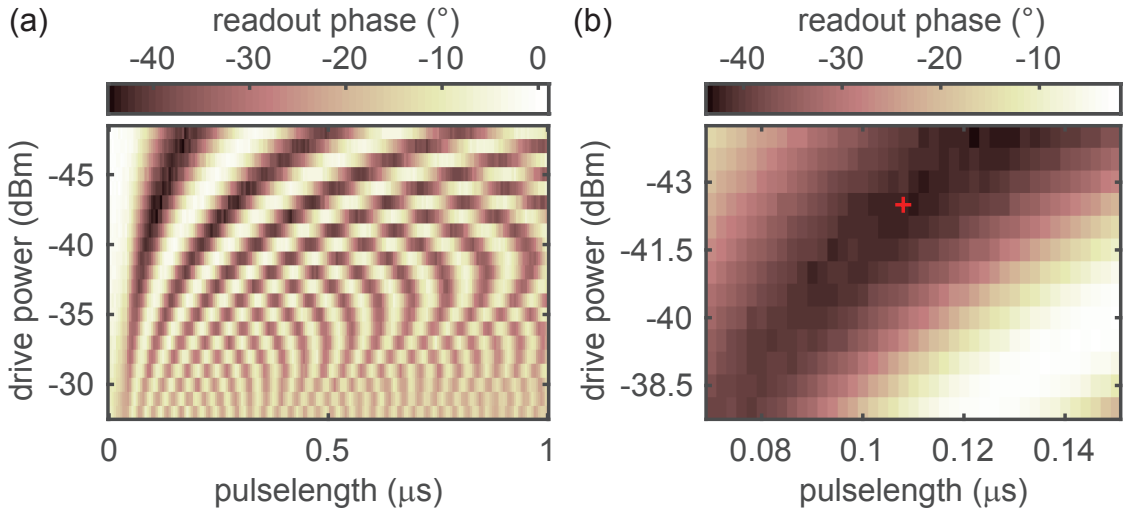

Figure 4.3: Readout phase measured following a drive pulse at qubit transition frequency (6.0687 GHz) mapped for varying drive power and pulselength. The red dot in (b) indicates the optimum chosen by Hand.

Using our CMA-ES optimizer approach and taking the values of the handoptimized qubit π-pulse parameters as initial guess leads to better results. The optimization process is shown in Fig. 4.4 and Fig. 4.5 (a). Fig. 4.4 shows the parameter guesses of CMA-ES whilst Fig. 4.5 (a) shows the readout phase for each optimizer guess. We

achieve convergence within approximately 300 iterations. The CMA-ES optimized parameters for our qubit π-pulse are listed in Tab. 4.1.
Focusing on parameter convergence in Fig. 4.4 we still recognize a considerably high variance for the drive power, pulselength and drive phase guesses after convergence of the readout phase in Fig. 4.5 (a). Those parameters have a shallow optimum in parameter space covered with noise preventing CMA-ES from tightening the sampling area defined by Eq. (4.2). We can explain this behavior by considering the readout phase in Fig. 4.5 (a) acting as objective function. After approximately 300 iterations, no significant change of the readout phase is visible. Thus, the effect of noise exceeds the effect of a small deviation in readout phase, leading to a constant sampling area with a fixed variance within the sampled parameter guesses in Fig. 4.4.

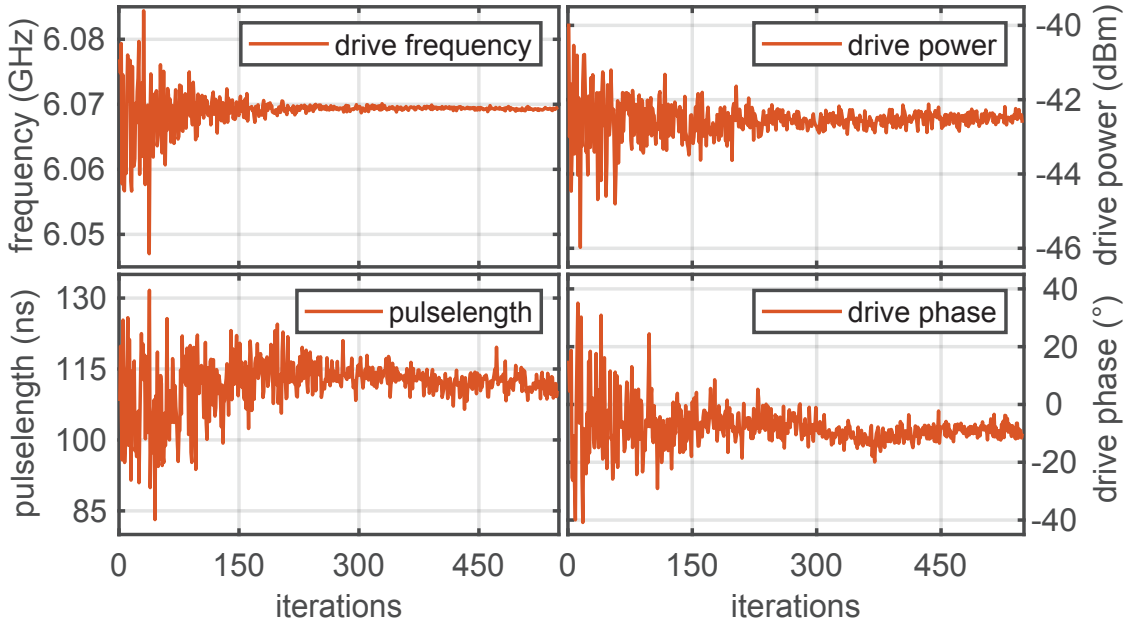

Figure 4.4: Parameter guesses of CMA-ES algorithm optimizing a qubit π-pulse.

In Tab. 4.1, a direct comparison between the handoptimized and the CMA-ES optimized π-pulse parameters is shown. We want to highlight that, in comparison to our previously measured qubit frequency in Fig. 3.8, the drive frequency of our optimized pulse is positively detuned by an amount of 0.6 MHz. This behavior occurred at multiple optimization runs and can thus not be assigned to a temporal change of the qubit transition frequency.
One possibility for that positive detuning of our qubit drive frequency might be the prevention of driving parasitic transitions. For transmon qubits, those occur at lower frequencies than our desired $|g\rangle$ to $|e\rangle$ qubit transition frequency. Detuning the drive also leads to an increased detuning of those transitions. Since our optimizer

is mainly interested in a high readout phase, the higher drive frequency might be a tradeoff with a (to be confirmed) positive impact on our gate fidelity.

Qubit π-pulse	pulselength	drive power	drive frequency	drive phase
Handoptimized	108 ns	-42.5 dBm	6.0687 GHz	0°
CMA-ES optimized	112 ns	-42.5 dBm	6.0693 GHz	$-8.85°$

Table 4.1: Comparison of handoptimized and CMA-ES optimized qubit π-pulse parameters.

To visualize the differences between the handoptimized and the CMA-ES optimized π-pulse, we evaluate each pulse 100 times in order to obtain sufficient statistics. In Fig. 4.5 (b), the distribution results of those measurements with their gaussian fits are shown. Using the optimized pulse leads to an increase of the readout phase magnitude of approximately 2.6%.

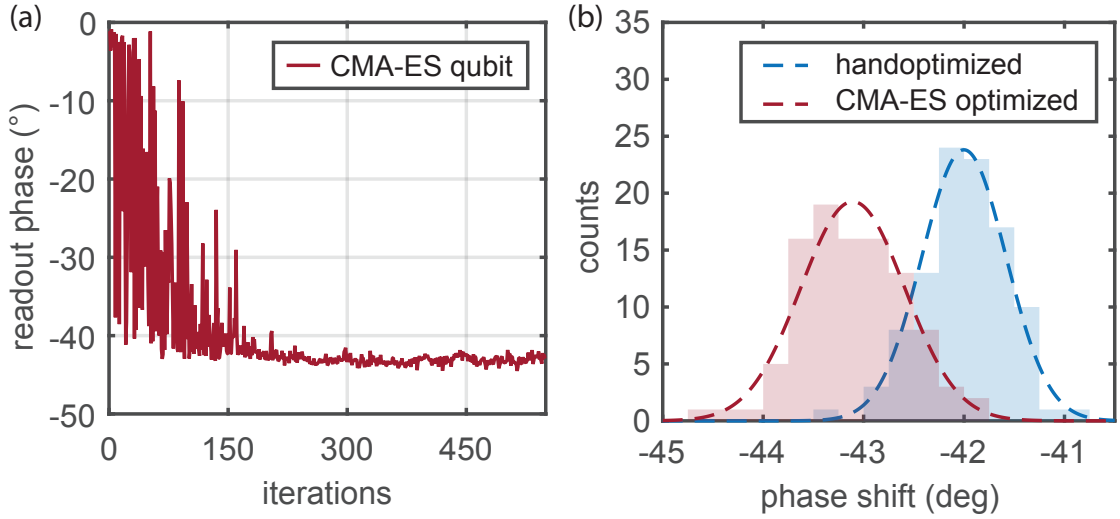

Figure 4.5: (a) Readout phase measured following a qubit pulse with parameters from CMA-ES guess for increasing CMA-ES iteration number (evaluated candidates). In (b), readout phase statistics using handoptimized pulses $(-42.0 \pm 0.4)°$ and CMA-ES optimized pulses $(-43.1 \pm 0.5)°$ are compared.

To summarize the results in this section, we want to note that a CMA-ES optimized π-pulse exhibits a higher readout phase indicating a higher z-fidelity than our handoptimized π-pulse. Since the z-fidelity is only an indicator for the overall fidelity of a quantum gate, we perform Quantum State Tomography in Sec. 4.3.

4.2.2 BSB pulse optimization

The blue sideband transition, as indicated in Fig. 2.3, maps the $|g,0\rangle$ to the $|e,1\rangle$ state. When driving, the necessity of a two-photon process results in a transition frequency of $(\tilde{\omega}_\mathrm{B} + \tilde{\omega}_\mathrm{q})/2$ which is strongly power-dependent due to the stark shift [cf. Eq. (2.29)]. Thus, finding good parameters for the BSB π-pulse is challenging. In Fig. 4.6, the readout phase indicating the BSB transition is mapped versus drive power and drive frequency. We fix the pulselength to 80 ns for practical considerations. Considering the pulselength as additional parameter to be mapped would fail in terms of exceeding feasible measurement time.
In the region around 7.31 to 7.32 GHz the readout phase exhibits extraordinary high values due to some parasitic resonance which are cropped for visibility. Using a high-pass filter can circumvent this behavior[2]. For high drive power, the readout phase exhibits some minor deflection from zero independent of the frequency applied.
The optimum chosen by hand is marked with a red cross in Fig. 4.6 and the hand-doptimized π-pulse parameters are listed in Tab. 4.2.

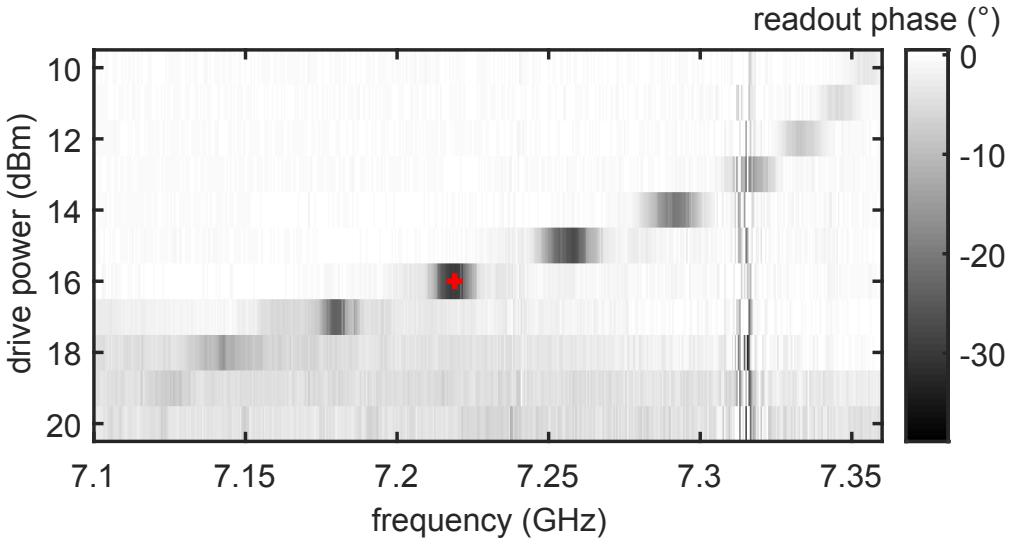

Figure 4.6: Readout phase measured following a BSB pulse mapped for varying drive power and drive frequency. The pulselength is fixed at 80 ns. The red cross indicates the optimum chosen by hand.

When considering CMA-ES for optimizing the BSB π-pulse, the deflection of the readout phase for high drive power can lead to a distraction. It results in a convergence at the high power boundary. To circumvent this behavior, the initial values

[2] We use a high-pass filter at the output port of the PSG RF source which has a cut-off frequency of 7.15 GHz

of the mean and the covariance matrix in Eq. (4.2) need to be set properly. The mean value should be close to the transition mapped by hand in Fig. 4.6 and the covariance matrix should have a sampling area which is approximately four times smaller than the frequency span shown in Fig. 4.6.
Starting with the handoptimized values as initial guess it takes the optimizer approximately 800 iterations to find the optimal π-pulse parameters. In Fig. 4.7 the BSB π-pulse parameter guesses are shown depending on the iteration number. The value of the pulselength parameter reaches its upper bound which is defined as 119 ns. The bound is considered for practical reasons: the full memory protocol should not exceed 500 ns regarding a qubit T_1-time of approximately 1.8 μs. This value hitting the boundary hints that longer π-pulses with less power result in a higher readout phase magnitude.

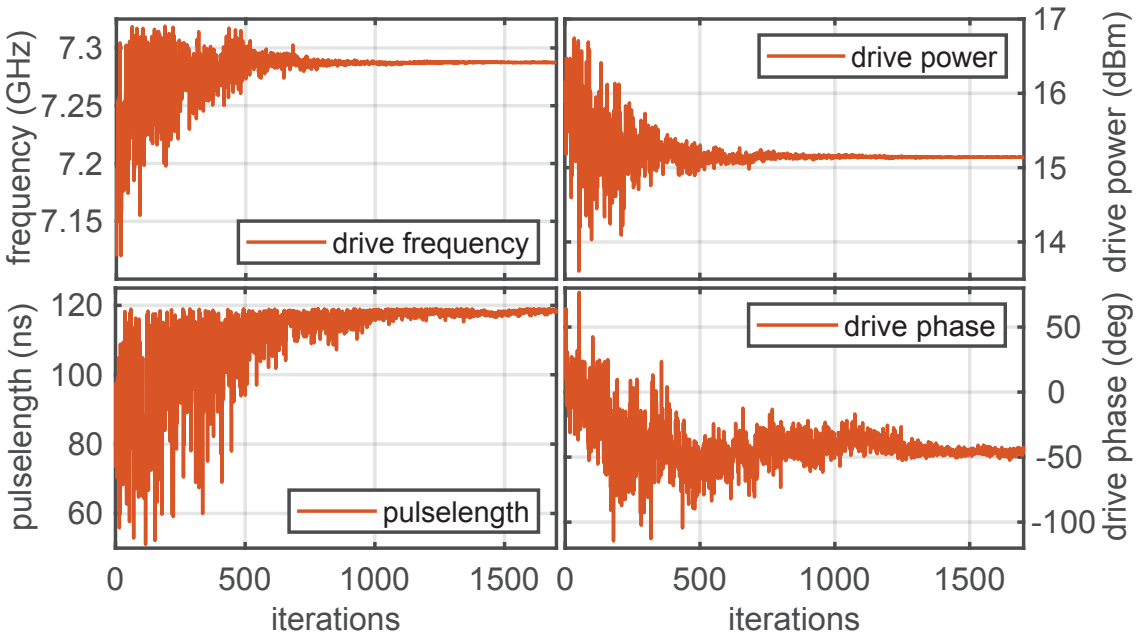

Figure 4.7: Parameter guesses of CMA-ES algorithm optimizing a BSB π-pulse.

In Fig. 4.8 (a), the BSB readout phase of the optimization run is shown depending on the iteration number. Compared to the maximum readout phase obtained by the qubit π-pulse optimization in Fig. 4.5 (a), the readout phase obtained by the BSB π-pulse is reduced. Due to the Stark shift altering the qubit transition frequency, the detuning Δ between qubit and readout mode decreases. This decrease in detuning leads to a change in the effective dispersive shift χ' between qubit and readout mode. Thus, we would expect an altered readout phase.
Figure 4.8 (b) shows the measured readout phase statistics for the handoptimized

case and the CMA-ES optimized case. The CMA-ES optimized case shows a significantly higher readout phase magnitude of approximately 19.1%.

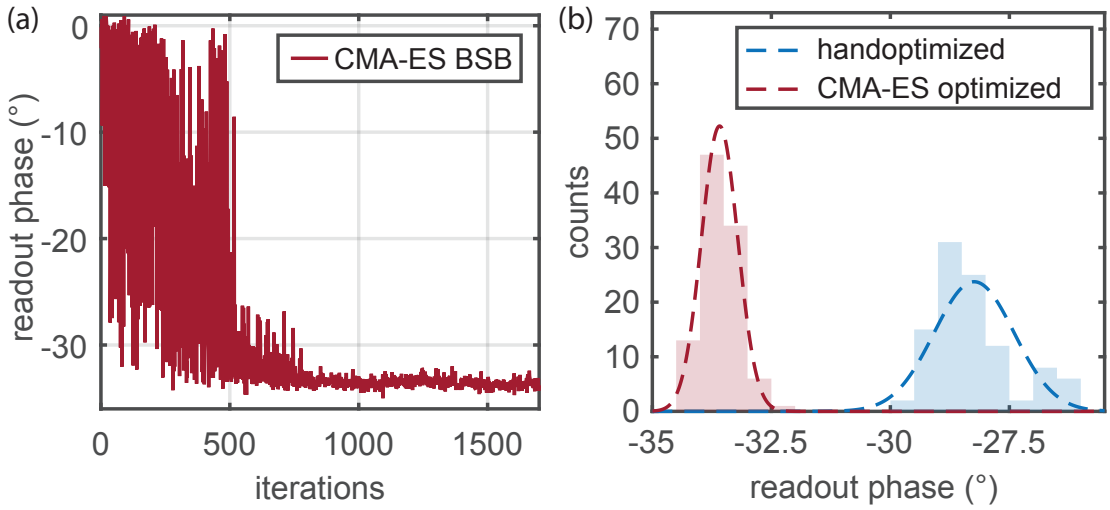

Figure 4.8: (a) Readout phase measured following a blue sideband pulse with parameters from CMA-ES guess for increasing CMA-ES iteration number (evaluated candidates). In (b), readout phase statistics using handoptimized pulses $(-28.2\pm0.8)°$ and CMA-ES optimized pulses $(-33.6\pm0.4)°$ are compared.

The optimal BSB π-pulse parameters resulting from the optimization run shown in Fig. 4.7 are listed in Tab. 4.2.

BSB π-pulse	pulselength	drive power	drive frequency	drive phase
Handoptimized	80 ns	16 dBm	7.219 GHz	0°
CMA-ES optimized	119 ns	15.1408 dBm	7.2874 GHz	−46.28°

Table 4.2: CMA-ES optimized qubit pulse parameters

Finally, the results above show that if optimizing the readout phase, CMA-ES can lead to better results in less amount of time. For the qubit π-pulse, the improvement is visible but not extraordinary. For the blue sideband π-pulse, the improvement is remarkable. Anyway, we expect the readout phase to be an indicator for the memory fidelity.

For the qubit, it has been shown in the past that for a given readout pulse (fixed frequency, power and duration), the higher the phase the better the fidelity of the $|0\rangle$ to $|1\rangle$ transition [18].

For the blue sideband, the high readout phase is less obviously related to a better memory fidelity because of the high drive power necessary for the two-photon process. This high power can lead to deflections of the readout phase without actually driving a desired transition. Furthermore, the Stark shift affecting our effective dispersive shift χ' needs to be considered. Thus, for the BSB transition, the readout phase might not be an ideal objective function to optimize for.
In order to test the performance of the CMA-ES optimized qubit π-pulses, Quantum Process Tomography (QPT) as described in Sec. 2.5.2 is applied and the results are shown in the next section.

4.3 Tomography with optimized qubit pulses

In this section, we present our results on performing quantum process tomography (QPT) on our optimized qubit pulses. The optimization of a qubit π-pulse is done as described in Sec. 4.1. By optimizing for two successive and identical pulses, we obtain an optimized $\pi/2$-pulse which is required for process tomography. To compare our result and highlight the improvement, we also show the expected result of a perfect π-pulse and the result of a simple hand-optimized pulse.

Theory π-pulse

As a first step, we show the real and imaginary part of the process matrix $\hat{\chi}$ for a perfect π-pulse acting as $\hat{R}_y^{\pi}$-Gate [cf. Eq. (2.11)] in Fig. 4.9. Each axis of the bar chart is labeled with the four operators forming our chosen operator basis (cf. Sec. 2.5.2). The only operator contributing is the $-i\hat{\sigma}_y$-operator defining a rotation around the y-axis of the Bloch Sphere by an angle of π.

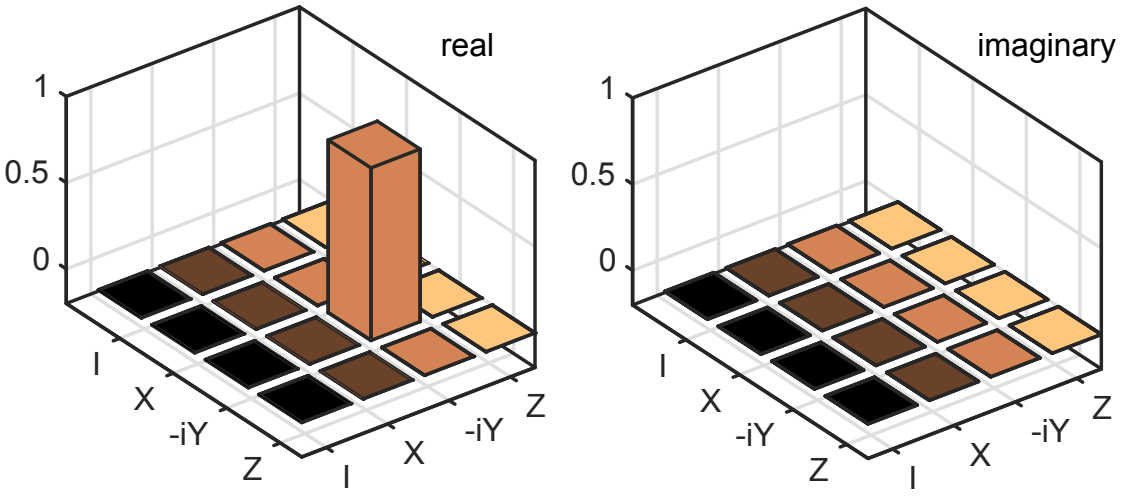

Figure 4.9: Real and imaginary part of theoretical process matrix representing a perfect π-pulse acting as $\hat{R}_y^{\pi}$-gate.

With the process matrix at hand, we have the opportunity to calculate the result of our quantum process acting on any input state by applying Eq. (2.38). In Fig. 4.10, a Bloch sphere representing a map of states $\hat{\rho}'$ as a result of our quantum process $\mathcal{E}_{\text{theory}}(\hat{\rho})$ is shown. A map of pure states $\hat{\rho}$ act as input states. Since our theory process matrix above does not contain any energy decay or dephasing, no distortions occur.

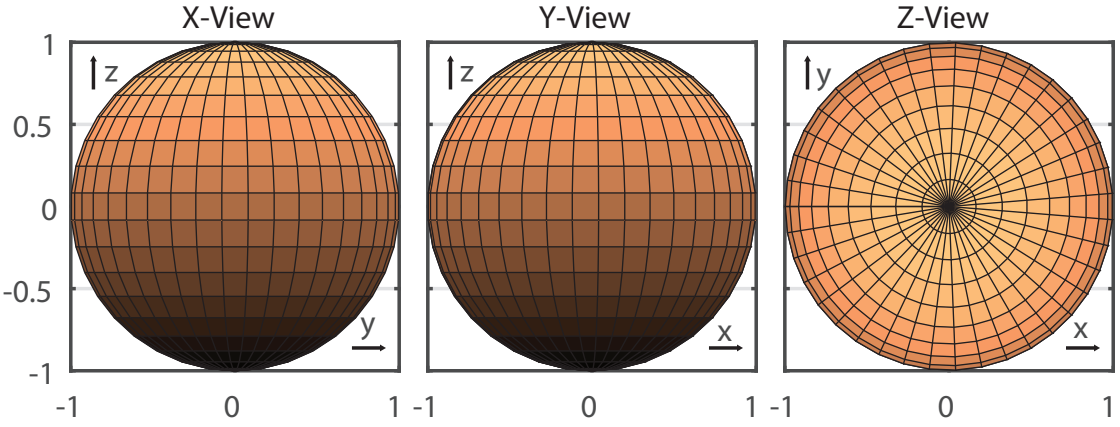

Figure 4.10: Bloch sphere map of quantum states $\hat{\rho}'$ obtained by applying our theory quantum process $\mathcal{E}_{\text{theory}}$ representing a perfect $\hat{R}_y^{\pi}$-gate to an initial map of pure quantum states $\hat{\rho}$.

Handoptimized π-pulse

For obtaining experimental quantum process matrices we need to follow the process tomography procedure described in Sec. 2.5.2.

We proceed by initializing our set of four initial states and applying our quantum process $\mathcal{E}$ which is our handoptimized π-pulse to be benchmarked. In Fig. 4.11 the real and imaginary part of the resulting process matrix for the handoptimized π-pulse is shown.

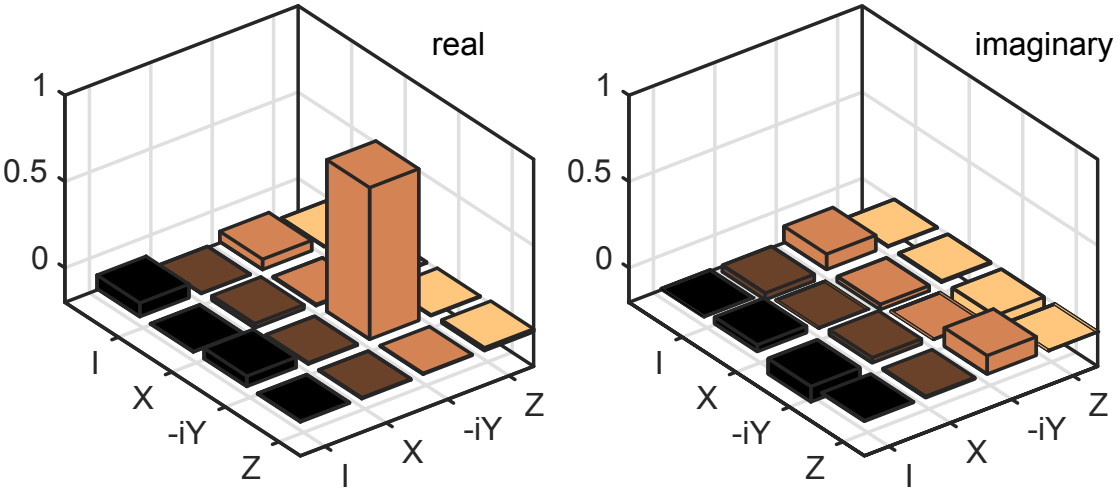

Figure 4.11: Real and imaginary part of experimental process matrix obtained by applying QPT to our handoptimized π-pulse acting as $\hat{R}_y^{\pi}$-gate.

In contrast to the expected result for a perfect π-pulse shown in Fig. 4.9, other operators than $-i\hat{\sigma}_y$ contribute.

In order to see distortions on the Bloch sphere, we again apply our reconstructed quantum process to a map of density matrices. The result can be seen in Fig. 4.12. Compared to the theory Bloch sphere in Fig. 4.10, deviations occur due to non-perfect pulses in experiment. It is clearly visible that the axis of the reconstructed sphere is not in parallel with the z-axis. This is an indicator for a deviation in the pulselength, leading to an unfinished rotation. Another artifact that occurs is the compression of the sphere along the x-axis which is attributed to dephasing effects.

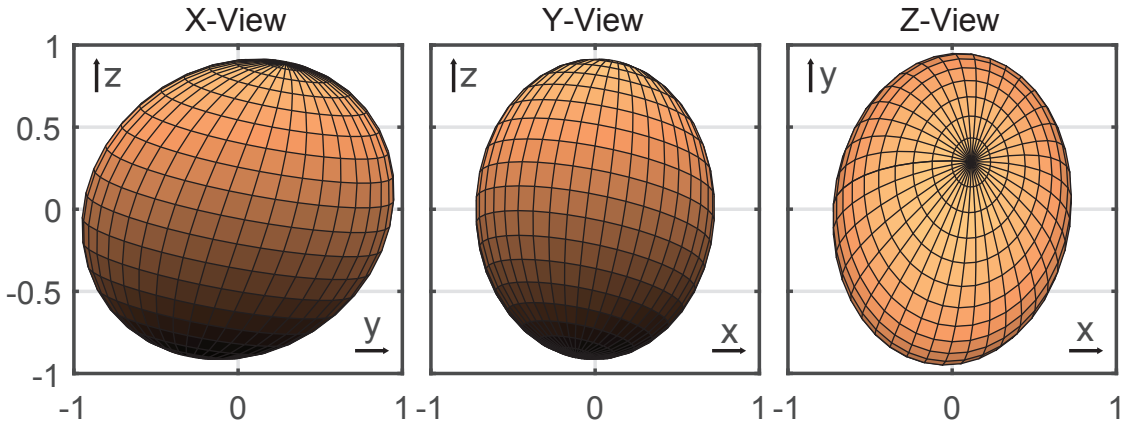

Figure 4.12: Bloch sphere map of quantum states $\hat{\rho}'$ obtained by applying quantum process $\mathcal{E}_{\text{handoptim}}$ to an initial map of pure quantum states $\hat{\rho}$.

Using Eq. (2.46), we can calculate the fidelity as a measure of similarity between the theory process matrix in Fig. 4.9 and our experimentally measured process matrix in Fig. 4.11. The fidelity of our handoptimized qubit pulse is $\mathcal{F} = 0.9375$. This value is worse than the value 0.9705, obtained by M. Renger in Ref. [18]. Taking into account that we did not measure multiple process tomographies of qubit π-pulses during this thesis to select them for good results the fidelity seems reasonable.

CMA-ES optimized π-pulse

As a next step, we apply quantum process tomography to our CMA-ES optimized qubit π-pulse. In Fig. 4.13, the resulting process matrix is shown. In comparison to the previously shown process matrix of our handoptimized π-pulse in Fig. 4.11, the elements not contributing to a π-pulse are negligibly small.
In Fig. 4.14, the result of our quantum process acting on a initial Bloch sphere map consisting of pure states is shown. The sphere is almost an ideal sphere tilted by a small angle. In comparison to our handoptimized π-pulse in Sec. 4.3, the fidelity is significantly higher with a value of $\mathcal{F} = 0.9864$.

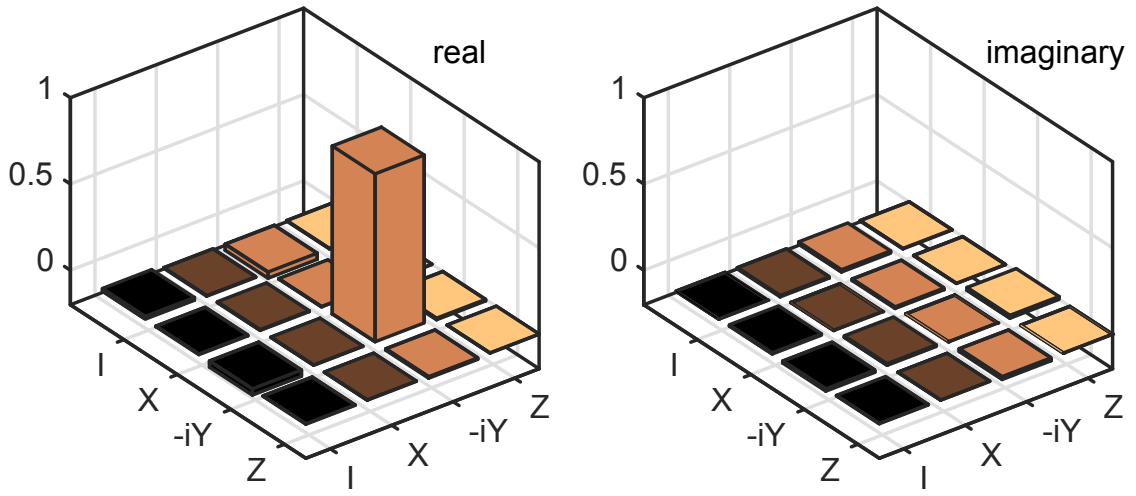

Figure 4.13: Real and imaginary part of experimental process matrix obtained by applying QPT to our CMA-ES optimized π-pulse acting as $\hat{R}_y^{\pi}$-gate.

Regarding the reconstructed Bloch sphere in Fig. 4.14, the only deviation that is clearly visible is a tilted z-axis. This tilt is a result of the finite detuning between the optimized pulse and the qubit transition frequency.

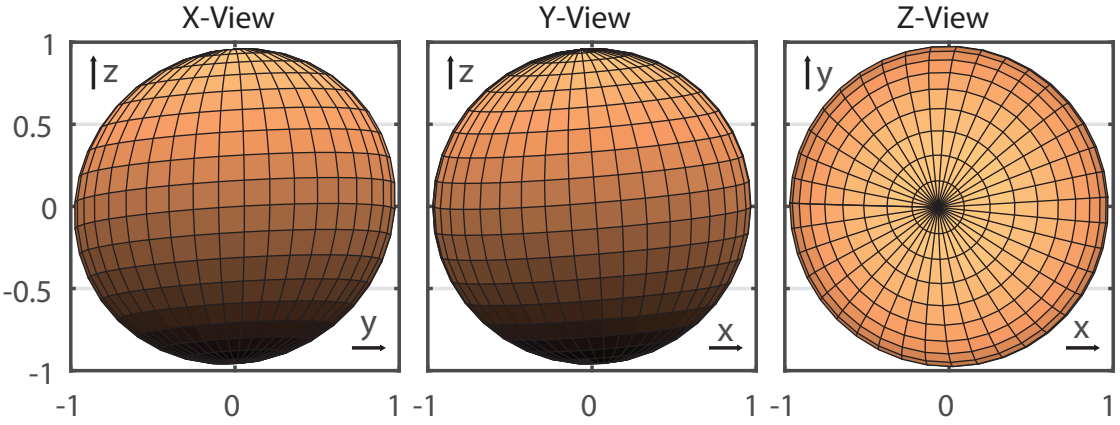

Figure 4.14: Bloch sphere map of quantum states $\hat{\rho}'$ obtained by applying quantum process $\mathcal{E}_{\text{CMA-ES}}$ to an initial map of pure quantum states $\hat{\rho}$.

Summarizing the results above, our optimal control engine using CMA-ES as an algorithm for optimizing simple flat-top gaussian qubit pulses leads to a significant increase of our process fidelity. For the blue sideband, process tomography was not applied.

4.4 Memory protocol and storage mode decay

In this section, we show our memory protocol storage time measurements and find out that they are not comparable to the previously measured storage times recorded for the same experimental setup. We further analyze the decay times of the cavity storage mode to find out that the memory time of our experiment is recently limited by a decay of the storage mode.

4.4.1 Memory protocol

We start our memory protocol measurements by finding a reasonable blue sideband pulse. Below the Rabi curves of two BSB pulses are plotted. The curves are measured using the PSG vector signal generator with an additional high-pass filter[3].

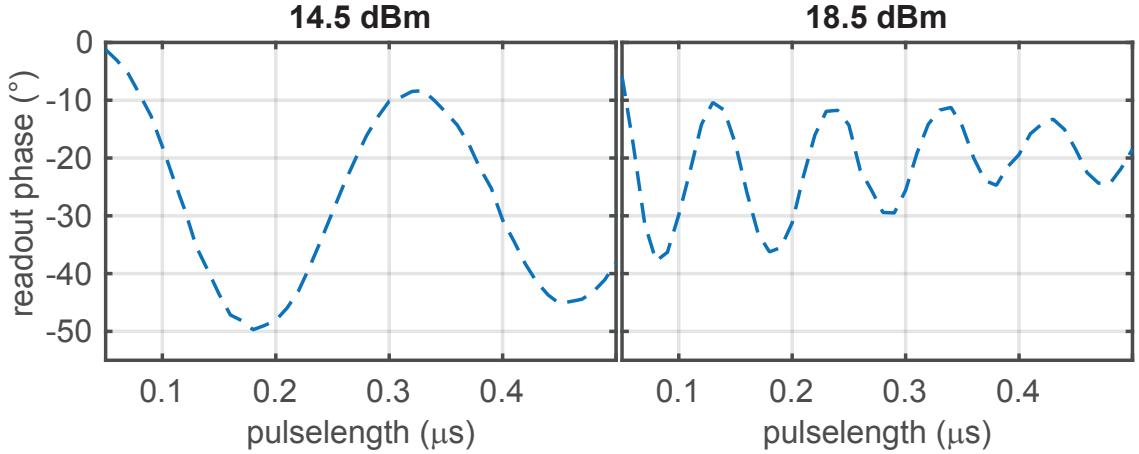

Figure 4.15: Readout phase measured following an applied drive at blue sideband transition frequency for two different drive power levels and varying pulselength. Those Rabi measurements are made for determining the relevant handoptimized π-pulse length. The high readout phase compared to Fig. 4.8 is due to an additional high-pass filter at the PSG RF output.

The blue sideband pulse with less power in Fig. 4.15 (14.5 dBm) leads to a significantly higher readout phase. Since we optimize for the readout phase (results shown in Sec. 4.2), our CMA-ES optimization algorithm would prefer the lower BSB drive power to the higher one.

The performance of our memory protocol is not benchmarked by the measured readout phase of a single pulse but by the fidelity of the process and the storage

[3] we use a high-pass filter at the output port of the PSG RF source which has a cut-off frequency of 7.15 GHz

time. In Fig. 4.16, the $T_{1,\mathrm{m}}$-time statistics of the memory protocol is shown. The BSB pulses used for the protocol are the same as in the Rabi plot in Fig. 4.15. The qubit pulses are the same for both cases and are performed using the R&S SGS100A RF source.

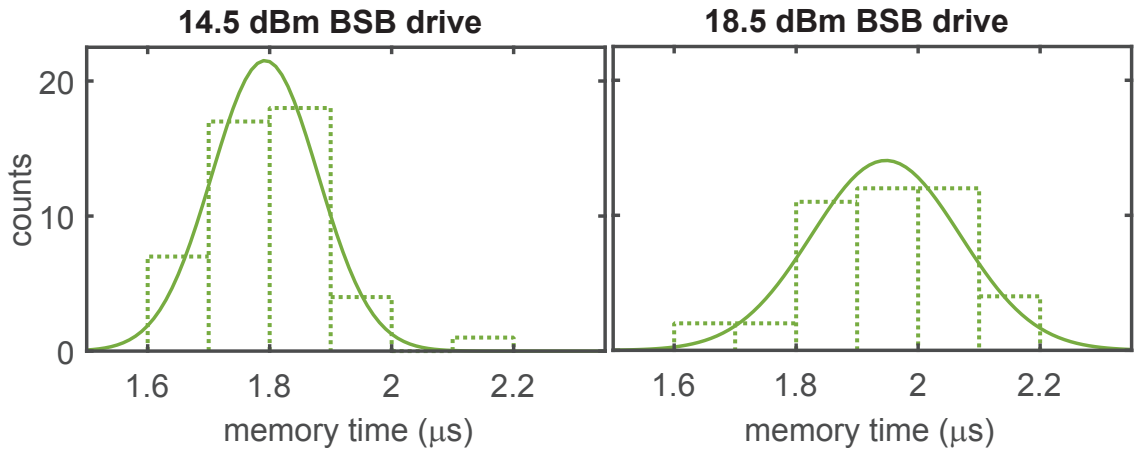

Figure 4.16: Memory time statistics for applied memory protocol. The two histograms use BSB π-pulses which differ in drive power but the same qubit π-pulse. A memory protocol with 14.5 dBm BSB drive power yields a memory time of (1.79 ± 0.09) μs and a 18.5 dBm BSB drive yields (1.95 ± 0.12) μs.

In Tab. 4.3, the mean and the standard deviation of the Gaussian distributions in Fig. 4.16 are shown. The difference in memory $T_{1,\mathrm{m}}$-time using two different BSB pulselengths indicates that a high readout phase does not automatically correspond to a good memory protocol performance. Thus, the readout phase used for optimization with CMA-ES as performed in Sec. 4.2.2 is not a good objective to optimize for.

drive power (dBm)	14.5	18.5
memory time $T_{1,\mathrm{m}}$ (μs)	1.79 ± 0.09	1.95 ± 0.12

Table 4.3: Mean and standard deviation of statistics recorded of Memory Protocol time displayed in Fig. 4.16.

In this thesis, we do not explore better objective functions further. The reason is as follows. Independently of the BSB drive power used, the decay times shown in Tab. 4.3 are much smaller than the decay times measured by Xie in [10]. In order to find out why our memory times decreased from 8 μs to below 2 μs, further measurements characterizing the storage mode are necessary.

We do so by measuring the decay time of the storage mode using a direct method in the next section.

4.4.2 Storage mode time domain measurements

Compared to the memory storage time of approximately 8 μs measured by the predecessors (E. Xie and M. Renger), our memory protocol measurement exhibits a significantly decreased storage time. The measurements shown below indicate that the decrease can be linked to a decreased memory mode lifetime.
In order to measure the lifetime of the storage mode directly, we make use of a specific measurement technique. For directly driving the mode, we apply a long drive pulse at the storage mode resonance frequency in order to ensure a constant number of photons in our storage mode. When turning that drive tone off, the mode decays. Immediatley after turning the drive tone off, we start probing our readout mode resonator. The fast decay of our readout mode ensures a proper mapping of the storage mode population.
In Fig. 4.17 (a), storage mode frequency sweeps are mapped versus varying drive power. This mapping allows us to determine the low-power limit for storage mode drive pulses in which we are capable of measuring the storage mode population in time.

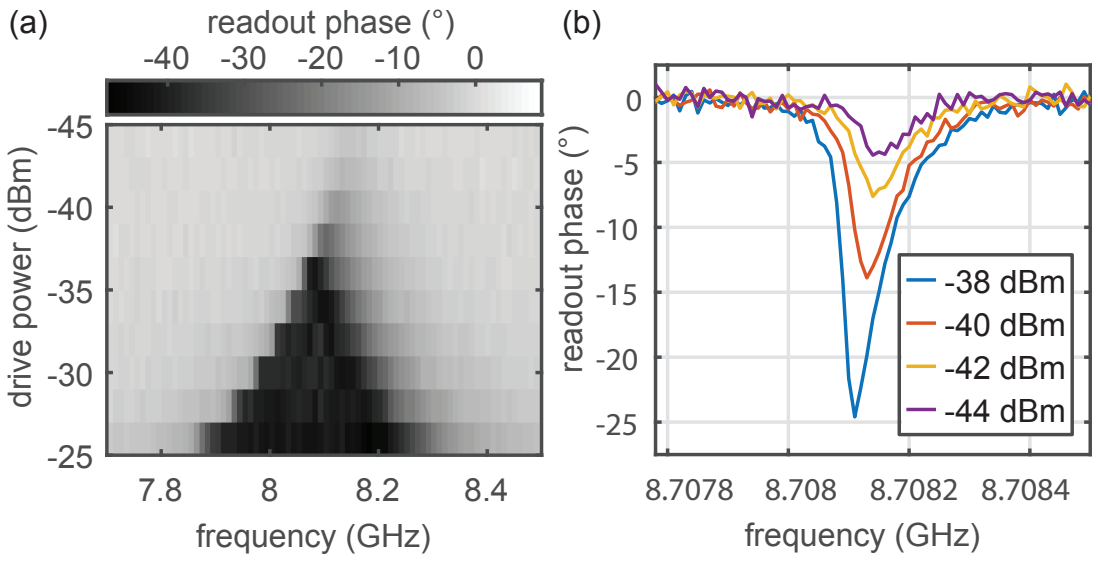

Figure 4.17: (a) Readout phase measured following a sufficiently long drive pulse close to the storage mode resonance frequency. The readout phase is mapped versus power and frequency of the applied pulse. (b) Readout phase for selected levels of low pulse power in (a).

In Fig. 4.17 (b), four of the frequency sweeps in (a) mapped in the low-power limit are shown individually. The peak of those curves indicates a storage mode drive on resonance for a given drive power. Plotting the time trace recorded by the FPGA-enhanced digitizer card at that frequency peak shows the exponential decay of the storage mode population.

In Fig. 4.18, a comparison between a storage mode decay recorded in 2017 [10] and a decay recorded during this thesis in 2019 is shown. The storage mode decay in 2019 with a lifetime of 1.4 μs is significantly shorter than the decay measured in 2017 with a lifetime of 9.2 μs. This decrease is the result for our short storage time shown in Fig. 4.16 when applying our memory protocol. To prevent confusion, we note that the differences in noise of the two decay curves are due to different averaging in the recording with the FPGA-enhanced digitizer card (cf. Sec. 3.1.5).

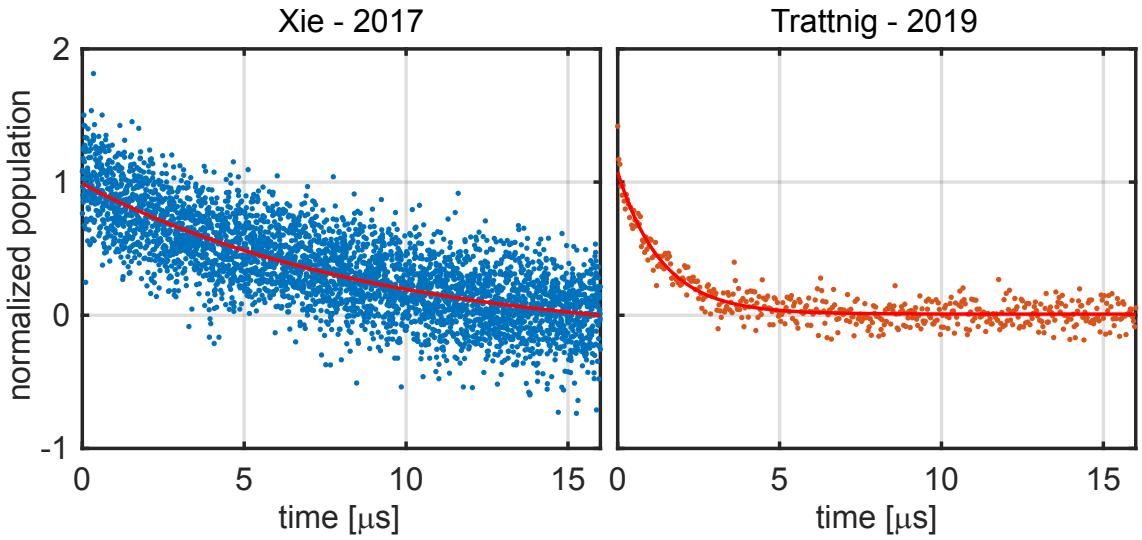

Figure 4.18: Comparison between storage mode decay times in 2017 and 2019. Blue data points are recorded in 2017 by Xie. An exponential fit results in a $T_{1,S}$-time of 9.2 μs. Red data points are recorded during this thesis in 2019, with a $T_{1,S}$-time of approximately 1.5 μs.

We proceed our storage mode measurements by measuring the storage mode lifetime using sufficient statistics. In Fig. 4.19 the histograms for decay time measurements with three different levels of drive power applied to the storage mode are shown.

drive power	-42 dBm	-40 dBm	-38 dBm
storage mode decay time $T_{1,\mathrm{S}}$ (μs)	1.57 ± 0.11	$1.47 \pm 0.07 s$	1.53 ± 0.09

Table 4.4: Mean and standard deviation of statistics recorded of storage mode decay time displayed in Fig. 4.19.

The mean storage mode decay time and the standard deviation of the histograms shown in Fig. 4.19 are listed in Tab. 4.4. The distributions do not differ significantly and indicate that a broadening in the frequency domain of our probed readout response in Fig. 4.17 occuring for increasing drive power does not affect the lifetime of our storage mode.

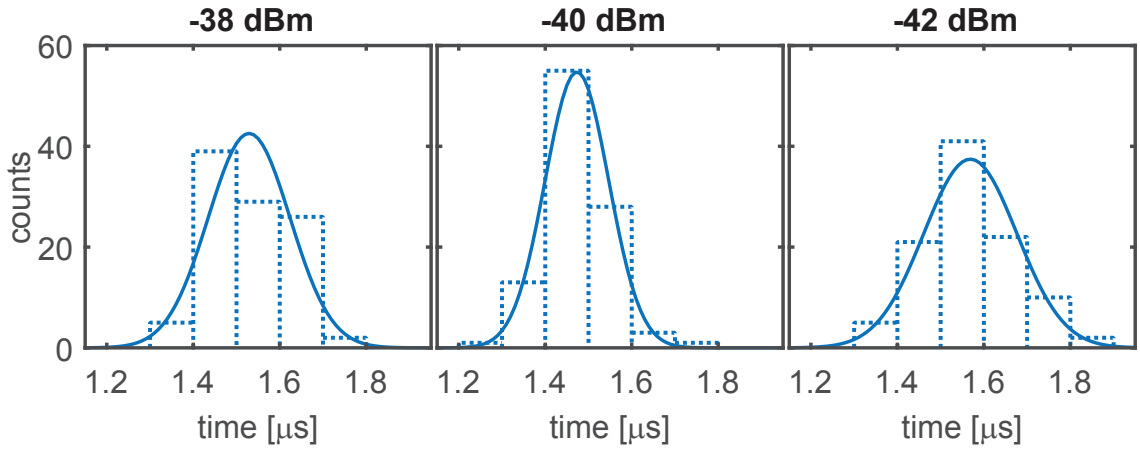

Figure 4.19: Storage mode decay time statistics obtained for three different levels of applied drive power at storage mode resonance frequency.

4.4.3 Storage mode frequency domain measurements

We continue to further investigate the storage mode in order to determine the reason for our memory underperformance. For three different cooldowns, we perform frequency sweeps with a VNA power of -70 dBm. In Fig. 4.20 those frequency sweeps are plotted.

The shape of the Lorentzian curves differs significantly within the cooldowns. We fit the three curves by using a resonator model allowing to correct for cross-coupling between the two resonator ports [49]. Quality factors and resonance frequencies obtained by fit are listed in Tab. 4.5. All three resonance curves show a significantly increased linewidth compared to the 24.7 kHz measured by E. Xie in 2017 [10].

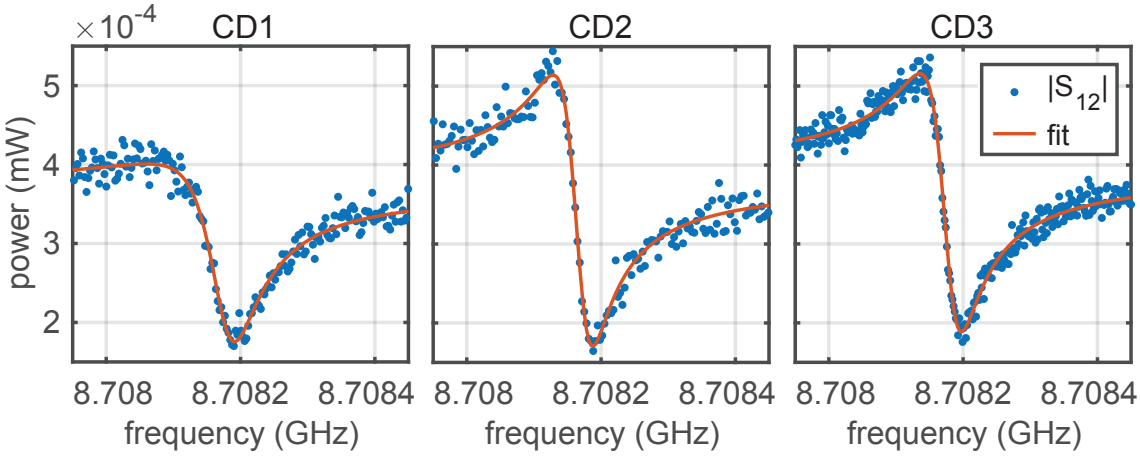

Figure 4.20: Blue points represent the reflected power when measuring the storage mode transmission close to resonance with a VNA for three different cooldowns (CD1-CD3). All three measurements are performed with -70 dBm VNA power and 1 Hz intermediate frequency. The low VNA power made averaging (N $\approx$ 10) crucial. Using a modified Lorentzian accounting for cross-coupling between the two resonator ports according to Refs. [49] to fit our transmission curves, we obtain the fit values listed in Tab. 4.5.

Using an underdamped oscillator model [52], we calculate the theory storage mode lifetime based on the linewidth of the resonance curve. The values are also listed in Tab. 4.5 and exceed the experimentally measured lifetime. The reason for this behavior is still unclear and requires further experiments beyond the time frame of this thesis.

Cooldown Nr.	1	2	3
quality factor	0.853×10^5	1.4765×10^5	1.4071×10^5
FWHM (kHz)	102	59	62
ν_S (GHz)	8.7081665	8.7081576	8.7081672
relative resonance	f1	f2 = f1-8.9 kHz	f3 = f1 + 0.7 kHz
$T_{1,S}$	1.5689	2.0726	1.4876
$T_{1,S}$ theory from Q-factor	3.118	5.397	5.1434

Table 4.5: Specific storage mode parameters measured for three different cooldowns.

Chapter 5

Conclusion and Outlook

Within this work, the main focus has been laid on optimizing pulseshapes for our quantum memory sample. As a main result, we can point out our implementation of a python-LabView interface allowing us to control our quantum memory experiment using a simple communication dictionary. We benefit from that interface in two ways. First of all, the remote control of the I and Q components of our pulsed microwave signal allows us to shape our pulses on a nanosecond timescale allowing more sophisticated pulseshapes than with our rigid "Deepthought" LabView program. The second positive effect that arises by swapping the pulse shaping from LabView to python is the possibility to use any python based optimal control technique. This includes optimization performed by CMA-ES throughout this thesis. It also enables access to our quantum memory experiment for our theory collaborators as well as the opportunity to use any python toolbox for optimization.

Another goal that has been achieved in this thesis is the proof of principle that optimization using the CMA-ES algorithm leads to better values for both, readout phase and overall quantum process fidelity for our qubit π-pulse. For the qubit π-pulse we have achieved an increase in gate fidelity, raising the value of $\mathcal{F} = 0.9705$ measured by M. Renger and E. Xie to a new high of $\mathcal{F} = 0.9864$ benchmarked by quantum process tomography. Optimization of the blue sideband has also led to promising results regarding the readout phase increase of 19.1% compared to our pulse optimized by hand.

Unfortunately, optimization on the full memory protocol has not been established due to some altering process of our memory sample. Thus, the last part of this thesis has focused on the storage mode, revealing a decreased lifetime. We have emphasized the decreased storage mode lifetime directly by VNA measurements yielding an increased linewidth. As a final result, we made this increased linewidth responsible for our short storage mode lifetime and directly link it to our memory

underperformance.
Even through optimizing our full memory protocol could not be implemented, this work can be regarded as a successful first step in achieving an optimized control of our compact quantum memory. The python-LabView interface offers the opportunity to control our experiment independent of our pulse generation setup. This enables future considerations in performing closed loop experiments for obtaining insight in theory [53], a testbed for optimized pulses [31] as well as simple application of complex pulse schemes.

Appendix A

Lab picture

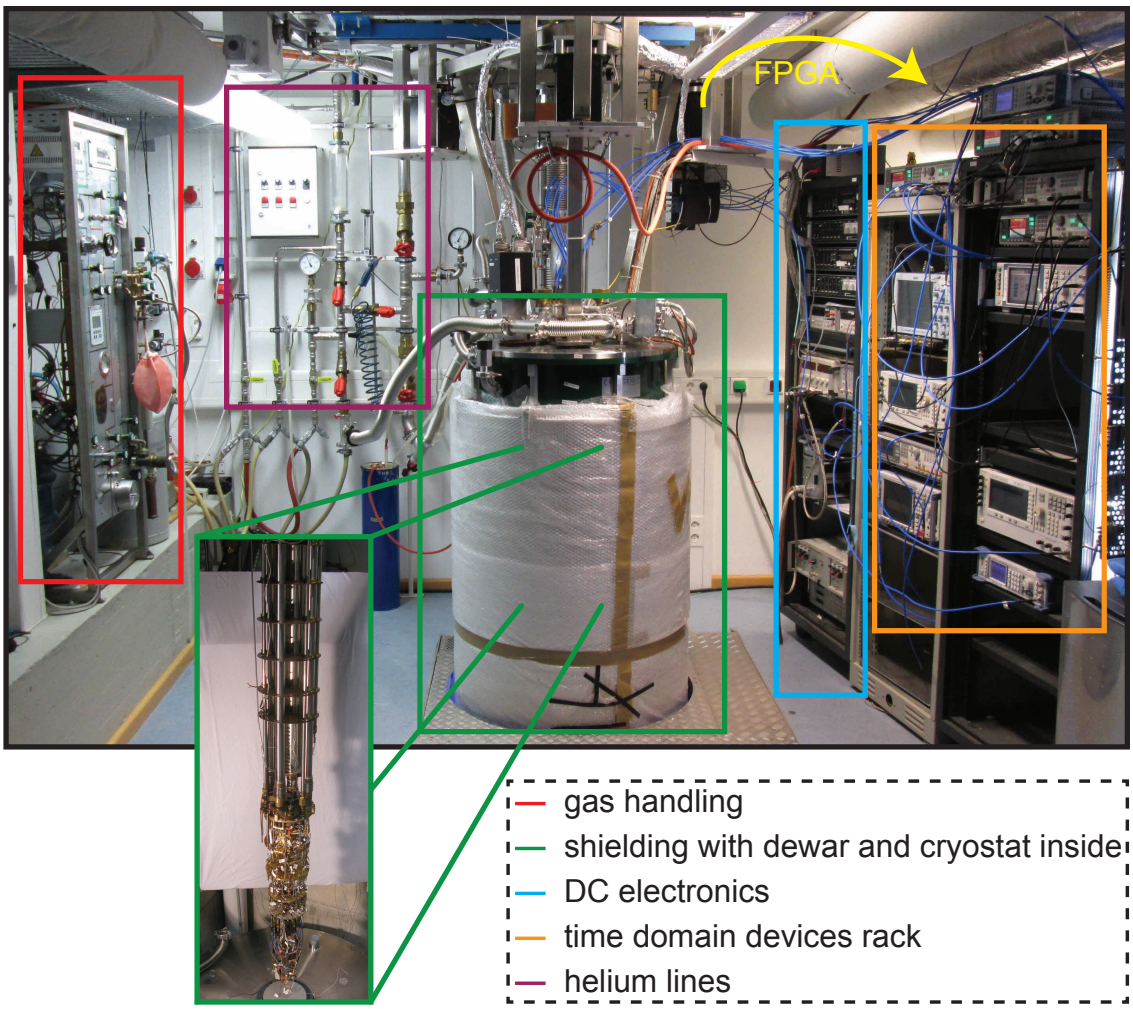

Figure A.1: Quantum memory experiment and lab equipment.

Bibliography

[1] A. Acín, I. Bloch, H. Buhrman, T. Calarco, C. Eichler, J. Eisert, D. Esteve, N. Gisin, S. J. Glaser, F. Jelezko, S. Kuhr, M. Lewenstein, M. F. Riedel, P. O. Schmidt, R. Thew, A. Wallraff, I. Walmsley & F. K. Wilhelm. The quantum technologies roadmap: a European community view. *New Journal of Physics* **20**, 080201 (2018). URL https://iopscience.iop.org/article/10.1088/1367-2630/aad1ea.

[2] A. K. Ekert. Quantum Cryptography and Bell's Theorem 413–418 (1992).

[3] L. K. Grover. A fast quantum mechanical algorithm for database search. *Japanese journal of human genetics* **41**, 333–338 (1996). URL http://arxiv.org/abs/quant-ph/9605043. 9605043.

[4] P. W. Shor. Polynomial-Time Algorithms for Prime Factorization and Discrete Logarithms on a Quantum Computer. *SIAM Journal on Computing* **26**, 1484–1509 (1997). URL http://epubs.siam.org/doi/10.1137/S0097539795293172. 9508027.

[5] S. Popescu, N. Linden & R. Jozsa. Quantum Information and Computation. *Journal of Physics A: Mathematical and General* **34**, 6723–6723 (2001).

[6] G. Wendin. Quantum information processing with superconducting circuits: a review. *Reports on Progress in Physics* **80**, 106001 (2017). URL https://iopscience.iop.org/article/10.1088/1361-6633/aa7e1a. 1610.02208.

[7] M. H. Devoret & R. J. Schoelkopf. Superconducting Circuits for Quantum Information: An Outlook. *Science* **339**, 1169–1174 (2013). URL https://www.sciencemag.org/lookup/doi/10.1126/science.1231930.

[8] J. M. M. et al. Quantum supremacy using a programmable superconducting processor. *Nature* **574**, 505–510 (2019). URL http://dx.doi.org/10.1038/s41586-019-1666-5http://www.nature.com/articles/s41586-019-1666-5. 1911.00577.

[9] E. Xie. A scalable 3D quantum memory. *PhD thesis* (2018).

[10] E. Xie, F. Deppe, M. Renger, D. Repp, P. Eder, M. Fischer, J. Goetz, S. Pogorzalek, K. G. Fedorov, A. Marx & R. Gross. Compact 3D quantum memory. *Applied Physics Letters* **112**, 202601 (2018). URL http://aip.scitation.org/doi/10.1063/1.5029514.

[11] P. J. Leek, M. Baur, J. M. Fink, R. Bianchetti, L. Steffen, S. Filipp & A. Wallraff. Cavity Quantum Electrodynamics with Separate Photon Storage and Qubit Readout Modes. *Physical Review Letters* **104**, 100504 (2010). URL https://link.aps.org/doi/10.1103/PhysRevLett.104.100504.

[12] M. Reagor, H. Paik, G. Catelani, L. Sun, C. Axline, E. Holland, I. M. Pop, N. A. Masluk, T. Brecht, L. Frunzio, M. H. Devoret, L. Glazman & R. J. Schoelkopf. Reaching 10 ms single photon lifetimes for superconducting aluminum cavities. *Applied Physics Letters* **102**, 192604 (2013). URL http://aip.scitation.org/doi/10.1063/1.4807015. 1302.4408.

[13] J. Werschnik & E. K. U. Gross. Quantum optimal control theory. *Journal of Physics B: Atomic, Molecular and Optical Physics* **40**, R175–R211 (2007). URL https://iopscience.iop.org/article/10.1088/0953-4075/40/18/R01. 0707.1883.

[14] S. J. Glaser, U. Boscain, T. Calarco, C. P. Koch, W. Köckenberger, R. Kosloff, I. Kuprov, B. Luy, S. Schirmer, T. Schulte-Herbrüggen, D. Sugny & F. K. Wilhelm. Training Schrödinger's cat: quantum optimal control. *The European Physical Journal D* **69**, 279 (2015). URL http://link.springer.com/10.1140/epjd/e2015-60464-1.

[15] S. Machnes, E. Assémat, D. Tannor & F. K. Wilhelm. Tunable, Flexible, and Efficient Optimization of Control Pulses for Practical Qubits. *Physical Review Letters* **120**, 150401 (2018). URL http://arxiv.org/abs/1507.04261{%}0Ahttp://dx.doi.org/10.1103/PhysRevLett.120.150401https://link.aps.org/doi/10.1103/PhysRevLett.120.150401. 1507.04261.

[16] J. M. Gambetta, F. Motzoi, S. T. Merkel & F. K. Wilhelm. Analytic control methods for high-fidelity unitary operations in a weakly nonlinear oscillator. *Physical Review A* **83**, 012308 (2011). URL https://link.aps.org/doi/10.1103/PhysRevA.83.012308. 1011.1949.

[17] Z. Chen, J. Kelly, C. Quintana, R. Barends, B. Campbell, Y. Chen, B. Chiaro, A. Dunsworth, A. G. Fowler, E. Lucero, E. Jeffrey, A. Megrant, J. Mutus, M. Neeley, C. Neill, P. J. J. O'Malley, P. Roushan, D. Sank, A. Vainsencher, J. Wenner, T. C. White, A. N. Korotkov & J. M. Martinis. Measuring and Suppressing Quantum State Leakage in a Superconducting Qubit. *Physical Review Letters* **116**, 020501 (2016). URL https://link.aps.org/doi/10.1103/PhysRevLett.116.020501. 1509.05470.

[18] M. Renger. *Quantum Process Tomography of a 3D Quantum Memory*. Master's thesis (2018).

[19] C. E. Shannon. A Mathematical Theory of Communication. *Bell System Technical Journal* **27**, 379–423 (1948). URL https://linkinghub.elsevier.com/retrieve/pii/S0016003223905065http://ieeexplore.ieee.org/lpdocs/epic03/wrapper.htm?arnumber=6773024.

[20] B. Schumacher. Quantum coding. *Physical Review A* **51**, 2738–2747 (1995). URL https://link.aps.org/doi/10.1103/PhysRevA.51.2738.

[21] M. A. Nielsen & I. L. Chuang. *Quantum Computation and Quantum Information* (Cambridge University Press, Cambridge, 2010). URL http://ebooks.cambridge.org/ref/id/CBO9780511976667.

[22] R. Gross & A. Marx. *Festkörperphysik* (De Gruyter, Berlin, Boston, 2018). URL http://www.degruyter.com/view/books/9783110358704/9783110358704/9783110358704.xmlhttps://www.degruyter.com/doi/10.1515/9783110559187.

[23] B. Josephson. Possible new effects in superconductive tunnelling. *Physics Letters* **1**, 251–253 (1962). URL https://linkinghub.elsevier.com/retrieve/pii/0031916362913690.

[24] A. Barone & G. Paternò. *Physics and applications of the Josephson effect*. UMI Out-of-Print Books on Demand (Wiley, 1982). URL https://books.google.de/books?id=FrjvAAAAMAAJ.

[25] A. Larkin, K. Likharev & Y. Ovchinnikov. Secondary quantum macrpscopic effects in weak superconductivity. *Physica B+C* **126**, 414–422 (1984). URL https://linkinghub.elsevier.com/retrieve/pii/0378436384901967.

[26] A. A. Houck, J. Koch, M. H. Devoret, S. M. Girvin & R. J. Schoelkopf. Life after charge noise: recent results with transmon qubits. *Quantum Information Processing* **8**, 105–115 (2009). URL http://link.springer.com/10.1007/s11128-009-0100-6. 0812.1865.

[27] Y. Nakamura, Y. A. Pashkin & J. S. Tsai. Coherent control of macroscopic quantum states in a single-Cooper-pair box. *Nature* **398**, 786–788 (1999). URL http://www.nature.com/articles/19718.

[28] J. Koch, T. M. Yu, J. Gambetta, A. A. Houck, D. I. Schuster, J. Majer, A. Blais, M. H. Devoret, S. M. Girvin & R. J. Schoelkopf. Charge-insensitive qubit design derived from the Cooper pair box. *Physical Review A - Atomic, Molecular, and Optical Physics* **76**, 1–19 (2007). 0703002.

[29] P. Krantz, M. Kjaergaard, F. Yan, T. P. Orlando, S. Gustavsson & W. D. Oliver. A quantum engineer's guide to superconducting qubits. *Applied Physics Reviews* **6**, 021318 (2019). URL http://aip.scitation.org/doi/10.1063/1.5089550. 1904.06560.

[30] N. Wittler. *Optimale Kontrolle für Quantenspeicher*. Master's thesis (2018).

[31] F. Motzoi, J. M. Gambetta, P. Rebentrost & F. K. Wilhelm. Simple Pulses for Elimination of Leakage in Weakly Nonlinear Qubits. *Physical Review Letters* **103**, 110501 (2009). URL https://link.aps.org/doi/10.1103/PhysRevLett.103.110501. 0901.0534.

[32] A. Blais, R.-S. Huang, A. Wallraff, S. M. Girvin & R. J. Schoelkopf. Cavity quantum electrodynamics for superconducting electrical circuits: An architecture for quantum computation. *Physical Review A* **69**, 062320 (2004). URL https://link.aps.org/doi/10.1103/PhysRevA.69.062320.

[33] D. Pozar. *Microwave Engineering* (Wiley, 2011), 4 edn. URL https://www.wiley.com/en-us/Microwave+Engineering{%}2C+4th+Edition-p-9780470631553.

[34] W. Demtröder. *Laserspektroskopie 2* (Springer Berlin Heidelberg, Berlin, Heidelberg, 2013). URL http://link.springer.com/10.1007/978-3-642-21447-9.

[35] A. Wallraff, D. I. Schuster, A. Blais, J. M. Gambetta, J. Schreier, L. Frunzio, M. H. Devoret, S. M. Girvin & R. J. Schoelkopf. Sideband Transitions and

Two-Tone Spectroscopy of a Superconducting Qubit Strongly Coupled to an On-Chip Cavity. *Physical Review Letters* **99**, 050501 (2007). URL https://link.aps.org/doi/10.1103/PhysRevLett.99.050501. 0703632.

[36] J. Goetz, F. Deppe, K. G. Fedorov, P. Eder, M. Fischer, S. Pogorzalek, E. Xie, A. Marx & R. Gross. Parity-Engineered Light-Matter Interaction. *Physical Review Letters* **121**, 60503 (2018). URL https://doi.org/10.1103/PhysRevLett.121.060503. 1708.06405.

[37] F. Deppe, M. Mariantoni, E. P. Menzel, A. Marx, S. Saito, K. Kakuyanagi, H. Tanaka, T. Meno, K. Semba, H. Takayanagi, E. Solano & R. Gross. Two-photon probe of the Jaynes–Cummings model and controlled symmetry breaking in circuit QED. *Nature Physics* **4**, 686–691 (2008). URL http://www.nature.com/articles/nphys1016.

[38] A. Blais, J. Gambetta, A. Wallraff, D. I. Schuster, S. M. Girvin, M. H. Devoret & R. J. Schoelkopf. Quantum-information processing with circuit quantum electrodynamics. *Physical Review A* **75**, 032329 (2007). URL https://link.aps.org/doi/10.1103/PhysRevA.75.032329http://arxiv.org/abs/cond-mat/0612038http://dx.doi.org/10.1103/PhysRevA.75.032329. 0612038.

[39] D. C. McKay, C. J. Wood, S. Sheldon, J. M. Chow & J. M. Gambetta. Efficient Z gates for quantum computing. *Physical Review A* **96**, 022330 (2017). URL https://link.aps.org/doi/10.1103/PhysRevA.96.022330. arXiv:1612.00858v2.

[40] D. F. Walls & G. J. Milburn. Effect of dissipation on quantum coherence. *Physical Review A* **31**, 2403–2408 (1985). URL https://link.aps.org/doi/10.1103/PhysRevA.31.2403.

[41] H. Haken & H. C. Wolf. *Atom- und Quantenphysik*. Springer-Lehrbuch (Springer Berlin Heidelberg, Berlin, Heidelberg, 2004). URL http://link.springer.com/10.1007/978-3-642-18519-9.

[42] F. Deppe, M. Mariantoni, E. P. Menzel, S. Saito, K. Kakuyanagi, H. Tanaka, T. Meno, K. Semba, H. Takayanagi & R. Gross. Phase coherent dynamics of a superconducting flux qubit with capacitive bias readout. *Physical Review B* **76**, 214503 (2007). URL https://link.aps.org/doi/10.1103/PhysRevB.76.214503.

[43] M. Howard, J. Twamley, C. Wittmann, T. Gaebel, F. Jelezko & J. Wrachtrup. Quantum process tomography and Linblad estimation of a solid-state qubit. *New Journal of Physics* **8**, 33–33 (2006). URL https://doi.org/10.1088/1367-2630/8/3/033http://stacks.iop.org/1367-2630/8/i=3/a=033?key=crossref.0052b1c64fadbfcdcdfd20ed588bf381.

[44] K. Kraus, A. Böhm, J. D. Dollard & W. H. Wootters (eds.) *States, Effects, and Operations Fundamental Notions of Quantum Theory*, Vol. 190 of *Lecture Notes in Physics* (Springer Berlin Heidelberg, Berlin, Heidelberg, 1983). URL http://link.springer.com/10.1007/3-540-12732-1.

[45] M. Neeley, M. Ansmann, R. C. Bialczak, M. Hofheinz, N. Katz, E. Lucero, A. O'Connell, H. Wang, A. N. Cleland & J. M. Martinis. Process tomography of quantum memory in a Josephson-phase qubit coupled to a two-level state. *Nature Physics* **4**, 523–526 (2008). URL http://www.nature.com/articles/nphys972.

[46] E. Xie. Optimized fabrication process for nanoscale Josephson junctions used in superconducting quantum circuits. *Master Thesis* (2013).

[47] J. Goetz. The Interplay of Superconducting Quantum Circuits and Propagating Microwave States. *PhD thesis* (2017). URL http://www.wmi.badw.de/publications/theses.htm.

[48] G. Frossati. Experimental techniques: Methods for cooling below 300 mK. *Journal of Low Temperature Physics* **87**, 595–633 (1992). URL http://link.springer.com/10.1007/BF00114918.

[49] N. Pompeo, K. Torokhtii, F. Leccese, A. Scorza, S. Sciuto & E. Silva. Fitting strategy of resonance curves from microwave resonators with non-idealities. In *2017 IEEE International Instrumentation and Measurement Technology Conference (I2MTC)* Vol. 211–6 (IEEE, 2017). URL http://ieeexplore.ieee.org/document/7969903/.

[50] G. Kirchmair, B. Vlastakis, Z. Leghtas, S. E. Nigg, H. Paik, E. Ginossar, M. Mirrahimi, L. Frunzio, S. M. Girvin & R. J. Schoelkopf. Observation of quantum state collapse and revival due to the single-photon Kerr effect. *Nature* **495**, 205–209 (2013). URL http://www.nature.com/articles/nature11902. 1211.2228.

[51] N. Hansen. The CMA Evolution Strategy: A Tutorial (2016). URL http://arxiv.org/abs/1604.00772. 1604.00772.

[52] W. Demtröder. *Experimentalphysik 1*. Springer-Lehrbuch (Springer Berlin Heidelberg, Berlin, Heidelberg, 2015). URL http://link.springer.com/10.1007/978-3-662-46415-1.

[53] M. Werninghaus, D. J. Egger, F. Roy, S. Machnes, F. K. Wilhelm & S. Filipp. Leakage reduction in fast superconducting qubit gates via optimal control 1–8 (2020). URL http://arxiv.org/abs/2003.05952. 2003.05952.

Danksagung

Hiermit möchte ich mich bei allen Personen bedanken, die direkt oder indirekt zur Fertigstellung dieser Masterarbeit beigetragen haben.

An erster Stelle möchte ich Herrn Prof. Dr. Rudolf Groß für die Möglichkeit, diese Arbeit am Walther Meißner Institut zu absolvieren, danken. Seine inspirierenden Vorlesungen haben maßgeblich dazu beigetragen, mich für eine Masterarbeit am WMI zu entscheiden.

Allem voran natürlich auch meinem Betreuer Dr. Frank Deppe, der mir diese Arbeit ermöglicht hat und der sich trotz seines äußerst umfänglichen Arbeitsalltags als Gruppenleiter die Zeit genommen hat mir mit dem Experiment zu helfen. Auch seine umfangreichen Korrekturen waren hilfreich und haben die Qualität dieser Arbeit gesteigert.

Auch möchte ich mich bei meinem Vorgänger Edwar Xie bedanken. Wenn auch der Überlapp nur von kurzer Dauer war hat er mir innerhalb kürzester Zeit das für den Betrieb des Experiments benötigte Wissen vermittelt und stand auch nach seinem Abgang vom Walther-Meißner-Institut weiterhin für Fragen zur Verfügung.

Unerlässlich für diese Arbeit war selbstverständlich auch die Hilfe der Kollaborationspartner von der Universität des Saarlandes, Shai Machnes und Nicolas Wittler. Das für diese Arbeit programmierte Optimierungsprogramm trägt zu einem großen Teil ihre Handschrift. Auch konnten so einige Probleme in den gemeinsamen Videokonferenzen durch ihre Hilfe gelöst werden. Vielen Dank!

Nicht zu vergessen ist natürlich auch die Hilfe von Michael Renger, der das Projekt gemeinsam mit Edwar während seiner Masterarbeit kennen lernen durfte und die Quantenprozesstomographie als Messmethode implementiert hat. Auch seine Erklärungen bezüglich vielen Teilen des Experiments und seine Einführung in die Quantenprozesstomographie haben maßgeblich zur Entstehung dieser Arbeit beigetragen. Auch die Gespräche haben den Arbeitsalltag immer aufgehellt.

Bei meinen Bürokollegen Florian, Robert, Leander, Julia, Manuel und Raffael möchte ich ich für die vielen herzlichen Gespräche bedanken die einen den machmal doch frustrierenden Alltag eines Experimentalphysikers aufhellen. Hier seien natürlich auch die Doktoranden des WMI, allem voran Michael Renger und Stefan Pogorza-

lek erwähnt, die durch ihre verständnisvolle Art motivierend beitragen.

Natürlich besteht das Walther Meißner Institut aus mehr als nur Wissenschaftlern, die den täglichen Betrieb aufrecht erhalten. Auch diesen Personen sei gedankt. Hier sei auch speziell Dr. Kirill Fedorov für seine aufmunternden Worte erwähnt.

Nachdem ich bis hierhin lediglich Personen des Walther Meißner Instituts erwähnt habe, das Leben aber aus mehr als dem Arbeitsalltag besteht, möchte ich natürlich auch den Personen danken, die meinen bisherigen Lebensweg mit mir geteilt haben.

Allen voran natürlich meinen Eltern, Astrid und Josef, die mich auf all meinem Pfaden, die ich in meinem Leben beschritten habe, unterstützt haben. Ihr unerschütterlicher Glaube an mich gibt mir jeden Tag erneut den Ansporn, mein Bestes zu geben. Ohne ihre tatkräftige Unterstützung wäre diese Arbeit nie zustande gekommen. Diese Arbeit ist zu einem nicht zu unterschätzenden Anteil auch euer Verdienst.

Auch erwähnen möchte ich hier meine Freundin Alex, die in den arbeitsintensiven Zeiten des Schreibens zu mir gestanden hat und in dieser Zeit meinetwegen selbst auf viel verzichten musste.